

5-2012

Charging Kinetics of Micropores in Supercapacitors

Daniel Oberklein

Clemson University, dfoberklein@roadrunner.com

Follow this and additional works at: https://tigerprints.clemson.edu/all_theses

 Part of the [Mechanical Engineering Commons](#)

Recommended Citation

Oberklein, Daniel, "Charging Kinetics of Micropores in Supercapacitors" (2012). *All Theses*. 1347.
https://tigerprints.clemson.edu/all_theses/1347

This Thesis is brought to you for free and open access by the Theses at TigerPrints. It has been accepted for inclusion in All Theses by an authorized administrator of TigerPrints. For more information, please contact kokeefe@clemson.edu.

CHARGING KINETICS OF MICROPORES IN SUPERCAPACITORS

A Thesis Presented to
The Graduate School of
Clemson University

In Partial Fulfillment
of the Requirements for the Degree of
Master of Science
Mechanical Engineering

by
Daniel F. Oberklein
May 2012

Accepted by:
Dr. Rui Qiao, Committee Chair
Dr. Ardalán Vahidi
Dr. Xiangchun Xuan

ABSTRACT

The charging kinetics of Electric Double Layer Capacitors (EDLC) were studied using a continuum model based on the Poisson-Nernst-Planck (PNP) Equations, with the additional modeling of the bulk fluid motion in the electrolyte using the Navier-Stokes Equations. The results demonstrate that the addition of bulk flow modeling yields a faster charging rate and higher charging current due to the additional convective component of the current resulting from the bulk fluid motion. A parametric study was conducted to determine the effect of various physical parameters of the EDLC system on the charging kinetics. Decreased fluid viscosity results in a faster charging rate as the fluid velocities and, therefore, the convective current, becomes larger. Reduced ion mobility enhances the flow modeling effect by reducing the remaining non-convective components of the current, thus causing the convective current to represent a greater portion of the total current, but the penalty is lower overall current and correspondingly slower charging. Increased wall slip enhances the convective current by reducing friction at the walls and increasing the flow velocities. Widening the electrode pore bores increases charging rate by providing a greater cross-sectional area for the ion current to pass. Deepening the electrode pores slows the charging by requiring more ions to enter the pore in order to reach the steady-state charged condition.

TABLE OF CONTENTS

ABSTRACT.....	ii
TABLE OF CONTENTS.....	iii
1 INTRODUCTION	1
2 BACKGROUND AND THEORY OF THE ELECTRIC DOUBLE LAYER.....	5
2.1 Physical Descriptions of the EDL.....	5
2.2 The PNP Model.....	11
2.3 Navier-Stokes Equations.....	13
3 RESEARCH METHODOLOGY.....	14
3.1 Model Geometry	14
3.2 Physics Modules	19
3.3 Simulation Procedure.....	24
3.4 Postprocessing.....	32
4 RESULTS AND DISCUSSION.....	37
4.1 Illustration of the fluid and ion dynamics in the pore and channel system.....	37
4.2 Demonstration of the convective charging current effect.....	43
4.3 Effect of varying the solvent viscosity.....	47
4.4 Effect of varying the wall slip length.....	51
4.5 Effect of varying the ion mobility.....	56
4.6 Effect of varying the pore bore	63
4.7 Effect of varying the pore depth	67
4.8 Effect of varying the solvent density	71
5 CONCLUSIONS	74
APPENDIX.....	77
ENDNOTES AND REFERENCES.....	79

CHAPTER 1

INTRODUCTION

The Electric Double Layer (EDL) phenomenon is surprisingly widespread in occurrence, yet it is little known outside the academic and industry research communities. Essentially, the EDL is a layer of charge separation that occurs at a solid-liquid interface when sufficient free charge carriers (e.g., ions or free electrons) are present. The only requirements for formation of an EDL are sufficient free charge carriers and an electric potential to initiate the charge separation. The electric potential may be an externally-applied voltage, as seen in a capacitor or other electrochemical cell, or it may occur naturally as a result of inherent chemical potential differences in the ion species and the electrode material.

In a typical application where the EDL arises, a fluid medium containing mobile charge carriers is bounded by a solid surface. The fluid medium can be an electrolyte solution of positively-charged and negatively-charged ions dissolved in a solvent such as water. Alternatively, the fluid medium can be an ionic liquid. When an electric field is imposed across the fluid medium, the positively-charged ions migrate in the direction of lower electric potential, and vice versa. The electric field and resulting potential difference may arise naturally due to chemical interactions between the solid material and the fluid medium. For example, metal oxides often acquire a negative charge when immersed in water due to the dissociation of protons from hydroxyl groups on the oxide

surface ($\text{OH} \rightarrow \text{O}^- + \text{H}^+$) [9]. Alternatively, an electric field can be created within the fluid medium by applying a potential difference between the solid surface (electrode) and a counterelectrode, as would be done in charging a capacitor or operating an electromechanical device using electro-osmotic flow. In either case, the potential and resulting accumulation of charge on the solid surface causes counterions to be attracted to the fluid region adjacent to the solid surface, thereby screening the surface charge and tending to neutralize the electric field. The resulting charge on the solid surface, combined with the adjacent layer of opposite charge in the fluid medium, is referred to as the “electric double layer.”

The EDL sees applications in various electromechanical devices, including supercapacitors and electro-osmotic flow (EOF) devices. Perhaps the most widespread application, and the primary one of interest to the present investigation, is the supercapacitor. Also referred to as the Electric Double Layer Capacitor (EDLC), this capacitor is so named because it makes use of the EDL to accumulate charge in densities several orders of magnitude greater than ordinary parallel-plate and electrolytic capacitors, thereby providing greater energy density and much greater power density.[20][36]

The EDLC typically consists of two electrodes separated by a fluid medium containing mobile positive and negative ions. When an external potential is applied between the electrodes, a charge separation is induced by the electric field inside the fluid medium, with positive ions migrating to the region adjacent to the ground-potential electrode, and negative ions migrating to the region adjacent to the positive-potential

electrode. This results in an electric double layer forming at each electrode/electrolyte interface, where charge is stored.[20] In order to maximize the charge density within the electric double layer and accompanying surface charge density on the electrode surfaces, the electrodes are typically fabricated with numerous nanoscale pores into which the electrolyte can flow, resulting in a manifold increase in electrode/electrolyte interface surface area.[20][36] The porous electrodes are commonly made of activated carbon, which provides favorable pore dimensions and ages relatively slowly during use.[6][20] One relatively simple technique for forming electrodes with larger pores in the 100 nm range involves depositing a thin film of carbon black on the current collector [24], while carbon nanocages or carbon nanotubes can be used to obtain pores in the nanometer range.[13][22][44]

To better understand the role of the EDL in the operation of these devices, and to realize significant improvement in the performance of such devices, it is important to create accurate models of the EDL's formation and evolution. Particularly, we are interested in the kinetics of the charging and discharging of the EDL, which can be ascertained by studying metrics such as electric potential, charge density, and current density.

Prior efforts to model the EDL have generally fallen into two groups: continuum models, and molecular dynamics (MD) simulations. The continuum modeling approach has been performed using the Nernst-Planck equation to model the ion migration due to the electric field and diffusion, coupled with Poisson's equation to relate electric potential to charge density (Gauss's Law of electrostatics in differential form). In this thesis, the

PNP analysis will be carried a step further to include modeling of the bulk fluid motion using the Navier-Stokes equations. As will be seen, inclusion of the bulk flow model results in a more complete simulation of the charging kinetics that produces a discernible difference in the charging rate of the EDL.

Chapter 2 of this thesis will provide an overview of the relevant literature developing the theory of the electric double layer. Chapter 3 will describe the methodology used in the present investigation. Chapter 4 will present the data and results obtained, and Chapter 5 will offer conclusions drawn from this work.

CHAPTER 2

BACKGROUND AND THEORY OF THE ELECTRIC DOUBLE LAYER

2.1 Physical Descriptions of the EDL

The first attempt to provide a sound theoretical basis for the EDL was made by Helmholtz, who viewed the counterions as binding directly to the charged solid surface, forming a single layer of counterions that neutralize the charge on the solid surface. In this model, the single layer of counterions (referred to as the “Helmholtz layer”) completely balances and neutralizes the charge on the solid surface, leaving no electric field remaining in the liquid medium.[9] Thus, the remaining positive and negative ions within the bulk liquid outside the Helmholtz layer are uniformly distributed.

The Helmholtz model of the EDL was refined and improved upon by Gouy and Chapman in the second decade of the twentieth century. Gouy and Chapman added to the model by accounting for the random thermal motion of the ions, which causes ionic transport by diffusion throughout the fluid medium [9]. The effect on a concentrated region of ions, such as the Helmholtz layer, is to spread the region out into an extended region of charge. Accordingly, the Helmholtz layer becomes spread out into a diffuse region of smoothly-decreasing counterion concentration extending out into the bulk fluid. This new model is sometimes referred to as the “diffuse” model of the EDL or the

“diffuse EDL.” Figure 2.1 illustrates the counterion concentration profiles under the Helmholtz and Gouy-Chapman models of the EDL.

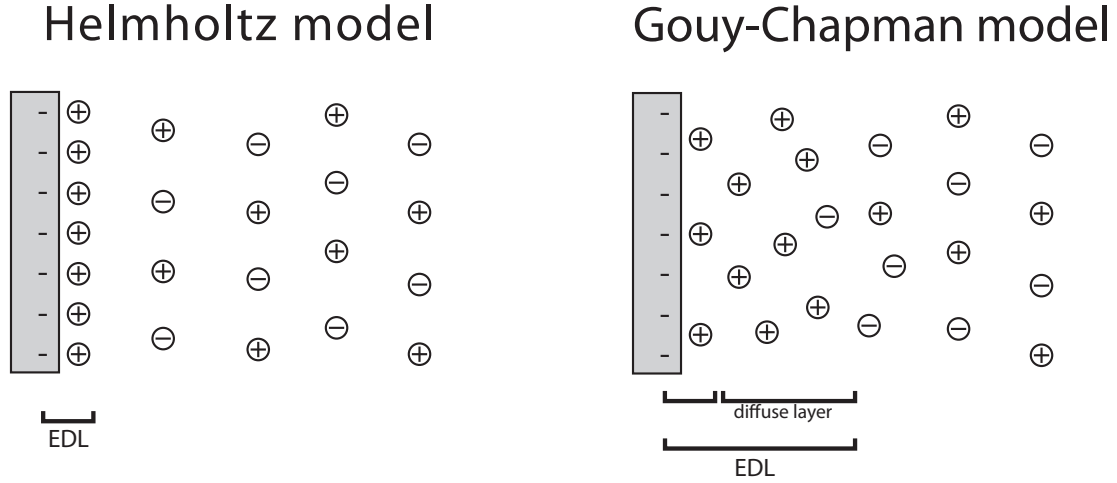


Figure 2.1: The Helmholtz and Gouy-Chapman models of the EDL

Under the diffuse theory of the EDL, the equilibrium distribution of counterions and, therefore, the electric potential in the EDL can be modeled using a Poisson-Boltzmann model. Gauss’s law of electrostatics, which is a form of Poisson’s equation, expresses the electric potential as a function of charge density:

$$\nabla^2 \phi = -\frac{\rho_e}{\varepsilon \varepsilon_0}$$

where ρ_e is the charge density at the point in question, ε is the permittivity of the medium, and ε_0 is the permittivity of a vacuum. To apply this law to the EDL, we invoke Boltzmann statistics, which holds that the ion distribution (specified as a concentration) of a species i is determined by the work needed to overcome the potential at the point in question:

$$c_i = c_i^0 \cdot e^{-W_i/k_B T}$$

where c_i^0 is the bulk concentration far away from the electrode, W_i is the work required to bring an ion of species i from zero potential to the point in question, and T is the temperature [9]. This work W_i is simply the ion charge multiplied by the potential:

$$W_i = z_i e \phi$$

Considering the case of two ion species, both monovalent with one having positive charge and the other having negative charge, the local charge density is given by [9]:

$$\rho_e = e(c_+ - c_-) = c^0 e \left[e^{\frac{e\phi}{k_B T}} - e^{-\frac{e\phi}{k_B T}} \right]$$

Substituting this expression for charge density into Poisson's equation, we have

$$\nabla^2 \phi = \frac{c^0 e}{\epsilon \epsilon_0} \left[e^{\frac{e\phi}{k_B T}} - e^{-\frac{e\phi}{k_B T}} \right]$$

This is the Poisson-Boltzmann equation, and it provides the steady state electric potential throughout the domain for a given set of electric potential boundary conditions and initial ion concentrations.[38]

The potential distribution for the EDL, as given by the Poisson-Boltzmann equation, is shown in Figure 2.2(a), and the ion concentrations in the EDL are shown in Figure 2.2(b).[11]

Recent research has suggested the presence of non-electrostatic effects originating in the so-called Yukawa pair potential on ion distribution in the EDL, but these effects were not modeled in the present study.[7]

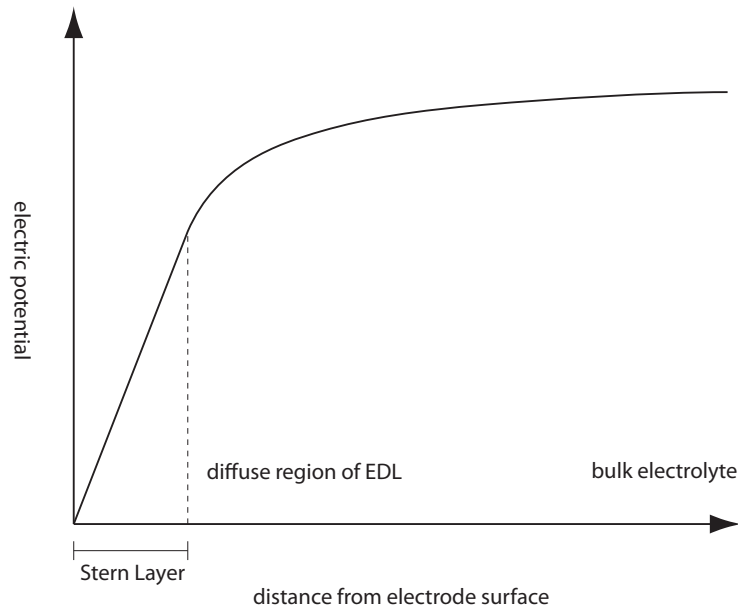


Figure 2.2(a): Electric Potential Function for Electric Double Layer

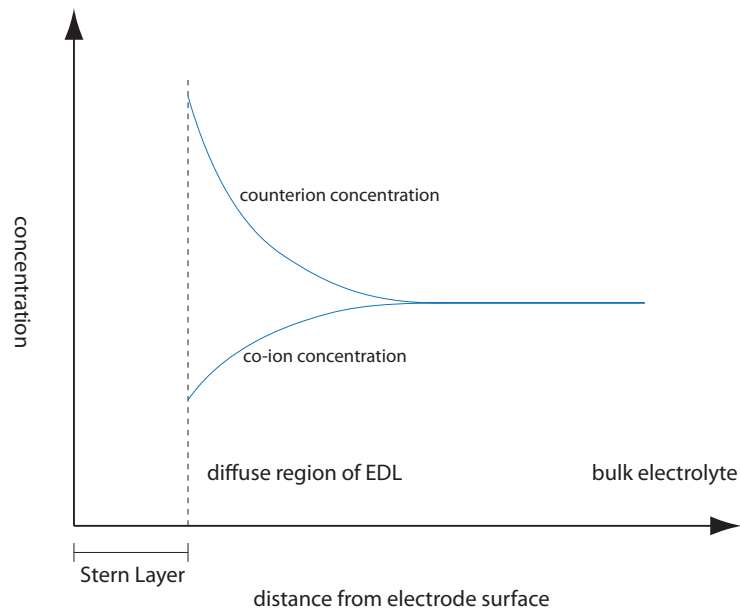


Figure 2.2(b): Ion Concentrations in the Electric Double Layer

The potential curve seen in Figure 2.2(a) is closely approximated by an exponential decay function of the form $\phi = \phi_0 e^{-kx}$, which provides a first-order approximation to the Poisson-Boltzmann equation and is valid for relatively low potentials [9]. The decay constant, k , provides a measure of the size of the EDL. The Debye length is defined [9] as

$$\lambda_D = k^{-1} = \sqrt{\frac{2e^2 c_0}{\epsilon \epsilon_0 k_B T}}$$

The Debye length gives a characteristic length by which the size of the EDL can be quantified. At a distance of λ_D from the electrode surface, the electric potential is $1/e$ as great as the potential on the electrode, using a hypothetical point infinitely far removed from the electrode as the reference “zero” point.

As a measure of the EDL’s size, the Debye length plays a critical role in indicating how much charge can be stored within the EDL. In fact, at low electric potential the capacitance of the EDL is:

$$C = \frac{\epsilon \epsilon_0 A}{\lambda_D}$$

where A is the surface area of the electrode [9][20]. This formula has exactly the same form as the familiar formula for the capacitance of a parallel plate capacitor:

$$C = \frac{\epsilon \epsilon_0 A}{d}$$

where d is the distance between the plates. Thus, the EDL behaves as a plate capacitor, with the diffuse layer of ions forming one of the “plates” on/in which charge of one polarity is stored.

The diffuse theory of the EDL was further refined by Stern, who reintroduced the Helmholtz notion of a single layer of ions adjacent to the solid surface. In Stern's theory, the EDL is viewed as comprising two parts: a single layer of ions that are directly adsorbed to the solid surface and are immobile, and a diffuse, outer layer of mobile ions extending out into the fluid bulk [9]. Unlike Helmholtz's model, in which the single layer of ions was equal and opposite in charge to the solid surface charge and therefore neutralized the latter, Stern's layer of charge is typically only a fraction of the magnitude of the charge on the solid surface, leaving an electric field extending into the fluid bulk, where it attracts additional counterions to form the diffuse portion of the EDL.[38] This duplex structure of the EDL under Stern's model is shown in Figure 2.3.

The specific adsorption of a layer of immobile ions to the solid surface results in a thin gap between the Stern layer of ions and the solid surface, the size of the gap being determined by the material properties of the ions, the solvent, and the solid. No ions can move closer to the solid surface than the Stern layer and occupy this gap.

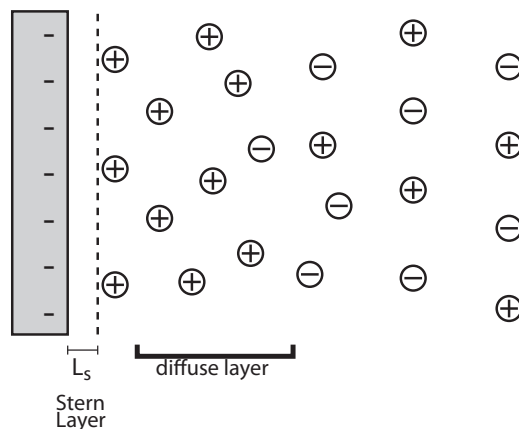


Figure 2.3: The Stern Layer

More will be said about the Stern layer and the thin gap in a later discussion of the simulation techniques used in the present investigation.

2.2 The PNP Model

Using the Gouy-Chapman diffuse model of the EDL as our descriptive guide, we wish to develop a mathematical treatment for the movement of ions over time. This will allow the charging kinetics of the EDL to be analyzed as the potential source is applied and the ions migrate to reach the equilibrium condition that characterizes the fully-charged EDL.

The general model for ionic transport in an electric field employs the Nernst-Planck equation:

$$\vec{J}_i = -D_i \vec{\nabla} c_i - \frac{z_i F}{RT} D_i c_i \vec{\nabla} \phi + c_i \vec{u}$$

This differential equation relates ion molar flux for species i to its concentration, the electric potential, and the fluid velocity at any point within the domain. In this equation, we have the following definitions:

- \vec{J}_i is the molar flux
- D_i is the diffusion coefficient
- c_i is the concentration
- z_i is the charge (in units of e) of ion species i .
- F is Faraday's constant ($F = N_A e$),
- R is the gas constant ($R = k_B N_A$)
- T is the temperature
- \vec{u} is the fluid velocity

The diffusion coefficient, D_i , for the ion species i is related to its mobility μ_i by the Einstein relation:

$$D_i = \frac{\mu_i k_B T}{z_i}$$

The Nernst-Planck equation consists of three terms representing the three fundamental transport phenomena that carry ions around within the domain. The first term, $-D_i \vec{\nabla} c_i$, is the diffusion term, which gives the ion flux due to thermal diffusion. The second term, $-\frac{z_i F}{RT} D_i c_i \vec{\nabla} \phi$, is the migration term, which gives the ion flux due to the electric field. The third term, $c_i \vec{u}$, is the convection term, which gives the ion flux due to transport by bulk fluid motion.

In applying the Nernst-Planck equation to an ionic solution or liquid, the electric potential ϕ will be determined by the charge density throughout the domain.

Mathematically, this can be expressed using Poisson's Equation, as previously discussed:

$$\nabla^2 \phi = -\frac{\rho_e}{\varepsilon \varepsilon_0}$$

where ρ_e is the charge density at the point in question, ε is the permittivity of the medium, and ε_0 is the permittivity of a vacuum. By combining this equation and the Nernst Planck equation, we have a model that allows us to determine ion flux using the known distribution of ions. This is known as the Poisson-Nernst-Planck (PNP) model, and it can be applied to model the evolution of ion distribution over time as ions are transported in response to the electric field, diffusion, and fluid motion.

2.3 Navier-Stokes Equations

At this point, a quick review of the above discussion will reveal that there is one parameter in the Nernst-Planck equation that has not yet been adequately specified: the fluid velocity, \vec{u} . In order to evaluate this term in the equation, we need a model for the fluid velocity throughout the flow field. That information is provided by the general equations of fluid motion, the Navier-Stokes equations.

$$\rho \frac{\partial u_j}{\partial t} + \rho u_k \frac{\partial u_j}{\partial x_k} = -\frac{\partial p}{\partial x_j} + \mu \frac{\partial^2 u_j}{\partial x_k \partial x_k} + \rho b_j$$

This equation is stated here in tensor form using index notation, and it represents three equations, one for each spatial dimension. The last term, ρb_j , is the body force term, and it represents forces whose action is distributed throughout an arbitrarily small element of volume within the fluid domain. In the current problem, the force exerted by the electric field on the ions contained within an element of fluid volume is modeled using this body force term.

As will be discussed below, the present investigation employs the Navier-Stokes equations to improve upon the standard PNP model by supplying the fluid flow solution needed to evaluate the fluid velocity that appears in the convective term of the Nernst-Planck ion transport equation. Research has not revealed any prior attempts to include this bulk fluid flow in the continuum modeling of the EDL. Accordingly, as discussed more fully below, the results of the present investigation show that inclusion of the bulk fluid motion does indeed have a discernible impact on the charging kinetics of the EDL.

CHAPTER 3

RESEARCH METHODOLOGY

The modeling and simulation of present investigation was performed using COMSOL Multiphysics version 4.1. The Nernst-Planck equation for ion transport was implemented using the Transport of Diluted Species physics module, which solves the Nernst-Planck equation without imposing an electroneutrality constraint at every point in the domain. Poisson's equation was implemented using the Electrostatics module, and the Navier-Stokes fluid flow modeling was implemented using the Laminar Flow module.

The primary goal of this investigation is to perform a parametric study of the PNP continuum simulation model with Navier-Stokes fluid flow modeling in order to ascertain the impact of the bulk fluid motion on the charging kinetics. For this parametric study, various parameters were studied, including ion mobility, solvent viscosity, solvent density, fluid boundary slip length, and electrode nanopore size. The charging kinetics were quantified using surface charge density on the electrode and electric current flowing through the electrode nanopore.

3.1 Model Geometry

The geometry used in the present modeling and simulations is shown in Figure 3.1. This geometry is intended to represent a device that stores electrical energy in the EDL, such as a supercapacitor. It consists of two electrodes separated by a channel region

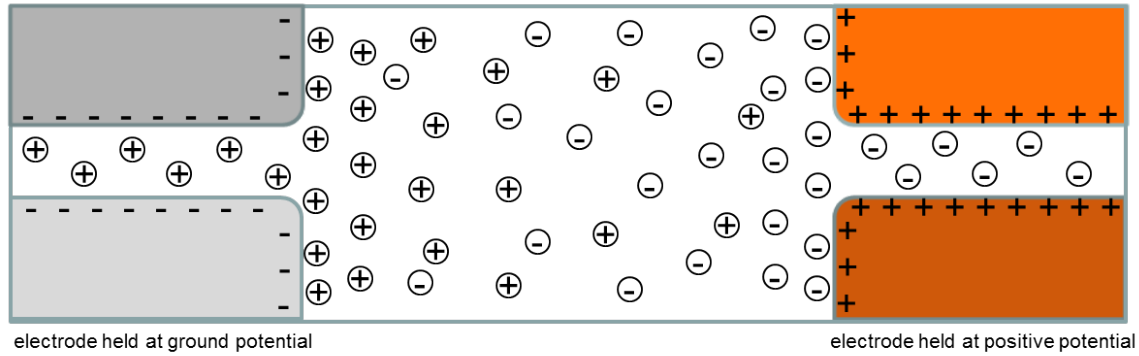
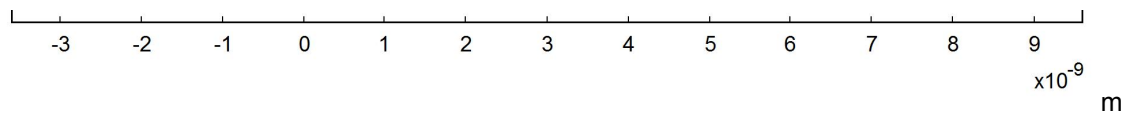


Figure 3.1: The model geometry

that is filled with an electrolyte solution containing equal numbers of positive and negative ions. When a potential difference is applied across the electrodes, ion transport within the electrolyte causes an EDL to form at each electrode/electrolyte interface as charge is transported and accumulates in those regions. Each of the two electrodes contains a nanopore bored into the electrode, into which electrolyte and ions can flow, thereby increasing the surface area of the interface and thus the amount of charge that can be accumulated in the EDL.[12] The nanopore used here represents a narrow slit whose breadth in the z -direction (into the page in these figures) is much greater than any of the other dimensions shown. This enables the problem to be modeled using a 2D geometry as shown here, with all numerical quantities being taken on a per-unit-breadth basis.

As can be seen from Figure 3.1, the 2D geometry of the present model also exhibits axial symmetry along a horizontal axis coinciding with the centerline of the electrode pores and the intervening channel. This symmetry allows the problem to be modeled using a domain consisting of half this area.



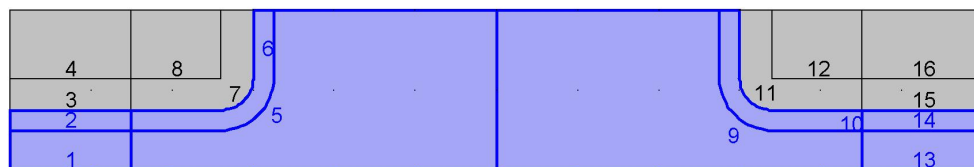
3.2(a): Subdomains of the problem geometry



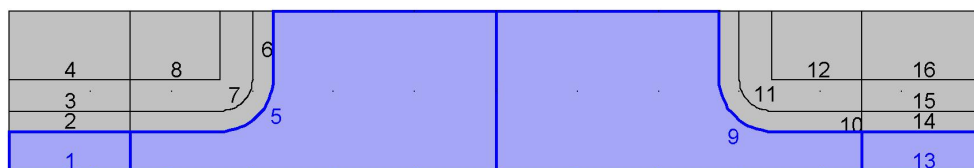
3.2(b): Electrodes



3.2(c): Stern Layer: thin low-permittivity gap



3.2(d): domain accessible to positive ions



3.2(e): domain accessible to negative ions

Figure 3.2: Geometry implementation in COMSOL

Figure 3.2 shows the problem geometry as implemented in COMSOL, where only the top half of the physical geometry of Figure 3.1 is used. The governing equations will be modeled and solved in this domain, with a symmetry condition being imposed along the entire bottom boundary of this half-geometry. This will accurately model the dynamics of the physical system, which is symmetrical in this manner.

Several additional refinements to the problem geometry were made in order to more accurately model the physical conditions that occur in the present problem. Figure 3.2(a) shows that the geometry has been partitioned into several subdomains. In Figure 3.2(b), the highlighted rectangles represent the solid electrodes, and the remainder of the domain area (not highlighted) represents the pore and channel regions occupied by electrolyte.

Figure 3.2(c) shows a thin gap highlighted adjacent to each electrode surface. This gap represents the Stern Layer, which is a thin low-permittivity gap between the solid electrode surface and the first layer of ions that are specifically adsorbed to the solid surface. Solvated ions are not free to enter this region. The Stern Layer typically has a relative electric permittivity ($\epsilon_r = \epsilon/\epsilon_0$) between 6 and 32 for water as solvent, because water molecules in this region are not free to rotate into the electric field [1][9]. For all simulations in the present study, a value of $\epsilon_r=7.8$ was used. The thickness of the gap represented by the Stern Layer in an aqueous electrolyte solution may be on the order of several Ångströms, depending on the ion species and the potential difference [9]. For the present study, a value of $L_s=0.4$ nm was used, which is appropriate for sodium and chloride ions in water with applied potentials no greater than 1 V [3][11].

An additional refinement to the model provides different boundaries for the mobile positive and negative ions. This accounts for the typically larger size of negative ions compared with positive ions, which means that the negative ions cannot be located as close to the solid surface of the electrode.[4][15][35] For example, various numerical simulations and X-ray diffraction studies have given a radius for the Na^+ ion of 0.95 Å to 1.02 Å, and a radius for the Cl^- ion of 1.81 Å to 1.98 Å, depending on the simulation and modeling method used [3][29]. Accordingly, the model allows for this fact that the Na^+ ions may be present approximately 1 Å closer to the electrode surface than the Cl^- ions. Figure 3.2(d) shows the highlighted domain accessible to the positive ions, which is essentially the entire pore-and-channel region, except for the aforementioned Stern Layer gap. Figure 3.2(e) shows the domain accessible to the negative ions. The 0.25 nm gap between the two domains is out-of-bounds to the negative ions.

These different domains for the positive and negative ions were implemented in COMSOL by using two different Transport of Diluted Species modules, one that operates on the positive ions, and one that operates on the negative ions. An additional effect of the EDL on electrical resistance to ion current caused by the tendency of a conductive current to balance the streaming ion current has been recently reported [18] but was not modeled in the present study.

3.2 Physics Modules

3.2.1 Ion Transport (Transport of Diluted Species)

As discussed above, the ion transport was modeled using the Nernst-Planck equation, as implemented by the Transport of Diluted Species physics module in COMSOL. Two separate copies of this physics module were used, one handling the positive ions, and one handling the negative ions. This allowed for the imposition of different boundaries, as shown in Figs. 3.2(d) and (e).

The boundary condition imposed on the Transport of Diluted Species physics was a no-flux condition on the Stern Layer boundary, as well as the ends of the pores and the channel top edge. These conditions are shown in Figure 3.3 for the positive and negative ion domains. These conditions model the “blocking” nature of the electrodes, as well as provide a closed fluid domain by preventing ions from escaping the ends of the pores or the top of the channel.

The symmetry condition, which is imposed along the entire bottom edge of the geometry for all the physics modules, is mathematically identical to the no-flux condition, providing that the gradient of the ion concentration flux in a direction normal to the boundary is zero, allowing no ion movement across the boundary.

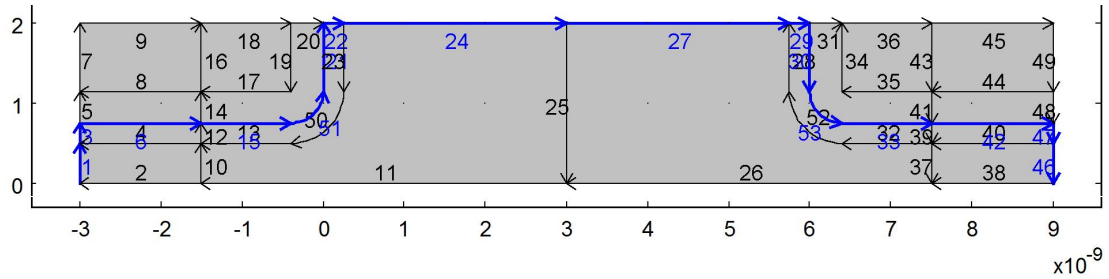
Recall the Nernst-Planck equation:

$$\vec{J}_i = -D_i \vec{\nabla} c_i - \frac{z_i F}{RT} D_i c_i \vec{\nabla} \phi + c_i \vec{u}$$

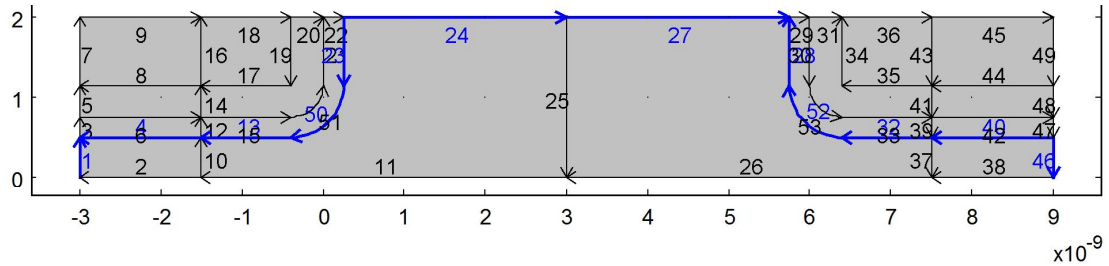
To compute values of the ion concentrations, c_+ and c_- , and the associated ion flux, $\vec{J}_{+,-}$, the physics module must be supplied with values of the electric potential, ϕ , and the fluid velocity, \vec{u} . In the present model, this information is provided by coupling to the other

physics modules: the Electrostatics module (Gauss's Law) solves for ϕ at each point in the domain, and the Laminar Flow module solves for \vec{u} .

The initial concentration was set at 2 M (2000 mol/m³) for the negative ions in all simulations. The initial concentration of the positive ions was calculated to provide equal numbers of positive and negative ions. Because the domain occupied by the positive ions is larger in volume, this means that the positive ion initial concentration was set lower than 2 M by a factor equal to the ratio of the areas of the two ion domains. These areas were determined by surface integration of the domains in COMSOL during a test run prior to the data collection simulations.



3.3(a): Positive ion no-flux boundary



3.3(b): Negative ion no-flux boundary

Figure 3.3: Boundary condition (no-flux) on the Nernst-Planck equation for the positive and negative ion species

3.2.2 Gauss's Law (Poisson's Equation)

For the implementation of Gauss's Law in COMSOL, the Electrostatics physics module was selected. The Electrostatics module is applied over the entire geometry of the problem because the electric potential within the electrolyte domain is determined by the conditions imposed on the other regions, from the point of potential application on the electrodes to the Stern Layer gap. These differing conditions governing the shape of the potential field are applied in much the same manner as boundary conditions, as discussed below.

The Electrostatics module requires that the spatial charge density be specified, in order for the module to solve for the electric potential. Within the pore and channel domains, which are accessible to the ions (positive or negative) as shown in Figure 3.2(d) above, the spatial charge density is specified in terms of the ion concentrations (c_+ and c_-):

$$\rho_e = (c_+ - c_-) \cdot F$$

As these are the dependent variables supplied by the Transport of Diluted Species module, they provide the model coupling between the Nernst-Planck equation and Poisson's equation. Additionally, the dielectric constant (or relative permittivity) must be specified. In COMSOL, this is done using a Charge Conservation condition for each domain. For water as solvent at standard temperature (25 °C) and pressure (1 atm), the dielectric constant is 78.41, and this value was used for all simulations in the present study. Accordingly, a Charge Conservation condition was applied to the electrolyte domains with a relative permittivity of 78.41.

For the gap representing the Stern Layer, highlighted in Figure 3.2(c) above, there are no ions present, and hence no charge carriers. Thus, the spatial charge density ρ_e is zero. A separate Charge Conservation condition was defined for this domain, and the dielectric constant for these regions was taken to be 7.8 for all simulations in the present study.

The domain representing the solid electrodes, highlighted in Figure 3.2(b) above, is modeled as a perfect conductor allowing charge to move freely across it, from the surface bounded by the electrolyte bath and Stern Layer to the distal edges, where the electrode would be connected to an external charge/discharge circuit. Accordingly, a spatial charge density of zero was used, along with a very high (10^4) dielectric constant.

The remaining boundary conditions implemented using the Electrostatics module are the applied electric potentials on the electrodes, which initiate the EDL charging process. These conditions will be discussed below with reference to the simulation procedures for this study.

3.2.3 Bulk Fluid Flow (Navier-Stokes equations)

For the modeling of the bulk fluid flow in COMSOL, the Laminar Flow physics module was selected. Examination of the Reynolds number for the flows seen in the simulations confirms that the flow may be treated as laminar. Typical maximum fluid velocities observed were around 2 m/s. The solvent viscosity was studied in the parametric study, and a value equal to one-tenth the viscosity of water (8.9×10^{-4} Pa·s) was used for many of the simulations; the physical support for such a value has support in

other studies, as discussed below. Taking the characteristic length dimension for the geometry as ~ 1 nm, these values give a Reynolds Number as follows:

$$Re_L = \frac{\rho v L}{\mu} = \frac{(1000)(2)(1 \times 10^{-9})}{(8.9 \times 10^{-4})(0.1)} = 0.0225$$

This Reynolds Number on the order of 10^{-2} is quite low indeed and is well within the laminar flow regime, and therefore is Stokes Flow.

The Laminar Flow module is coupled to the other physics modules in this model in two ways. First, as discussed above, it provides the fluid velocity data used by the Transport of Diluted Species module to solve for the ion concentrations. Second, the Laminar Flow module takes the ion concentration data as inputs and uses it to determine the body force (or volume force) that drives the fluid flow.

The physical model implemented by the Laminar Flow module in this problem works as follows: a parcel of fluid is pulled along as the ions within that parcel are subject to the electric force. Thus, the body force on the fluid is specified as follows:

$$\vec{F}_b = (c_+ - c_-) \cdot F \cdot (-\nabla\phi)$$

Another important condition that must be defined for the Laminar Flow module is the wall boundary condition, i.e., how the fluid motion behaves at the boundary with the solid electrode and channel wall surface. In addition to the familiar no-slip condition, various slip conditions were investigated in this study, as discussed below.

For all simulations in the present study, an initial fluid velocity of zero was used.

The Laminar Flow module also requires inputs of fluid density and viscosity. These values were varied as part of the parametric study; the values used and the results of such variation will be discussed fully below.

3.3 Simulation Procedure

The primary methodology used in the present investigation was to conduct a parametric study, varying different physical parameters that govern the model and examining the effects of different values of the parameters on the EDL charging rate and fluid motion. To this end, the simulations were conducted in groups, each group consisting of three or four simulations. Each group studied variation of one parameter, with the remaining parameters being held constant. In this manner, the effects of variation in that particular parameter could be ascertained. Each group typically included one or more simulations in which the Navier-Stokes fluid flow module was turned off, in order to obtain a PNP simulation without fluid flow modeling. This allowed comparison of the full simulation (PNP plus bulk flow modeling) with the standard no-flow PNP simulation in order to determine the manner and extent to which the addition of bulk flow modeling impacts the results.

3.3.1 General Simulation Overview

The simulation profile was designed to include two distinct phases. In Phase 1 of each simulation, no electric potential was applied across the electrodes; the ions and fluid were just allowed to move throughout their domain and reach an equilibrium condition.

This was necessary because the non-uniformities in the ion distribution caused by the different-size domains for positive and negative ions (as shown in Figure 3.2(d) and (e)) created an electric field in the vicinity of this domain gap along the electrode surface. The ions were allowed to redistribute themselves in order to reach an equilibrium condition that canceled out this electric field. Phase 1 typically lasted approximately 1 ns in the simulations; in some simulations it was 950 ps and in others it was 1025 ps, which values were chosen by experiment in order to allow COMSOL to converge to a solution and eliminate instabilities in the solver. Plots of the variables in Figure 3.4 show that the equilibrium condition was reached well in advance of this end of Phase 1.

In Phase 2 of the simulations, the electric potential was applied across the electrodes, and ions and fluid were allowed to move throughout their domain and reach a new equilibrium condition in which the EDLs were charged. A total simulation duration (Phase 1 plus Phase 2) of 3 ns was uniformly used in all simulations. This provided a duration for Phase 2 of between 1.925 ns and 2.05 ns. Plots of the variables in Figure 3.4 show that the EDL charged equilibrium condition was reached well in advance of the 3 ns endpoint of the simulations.

The implementation in COMSOL of the applied potential function, in which the applied potential was ramped up over a short period, is discussed in Appendix A.

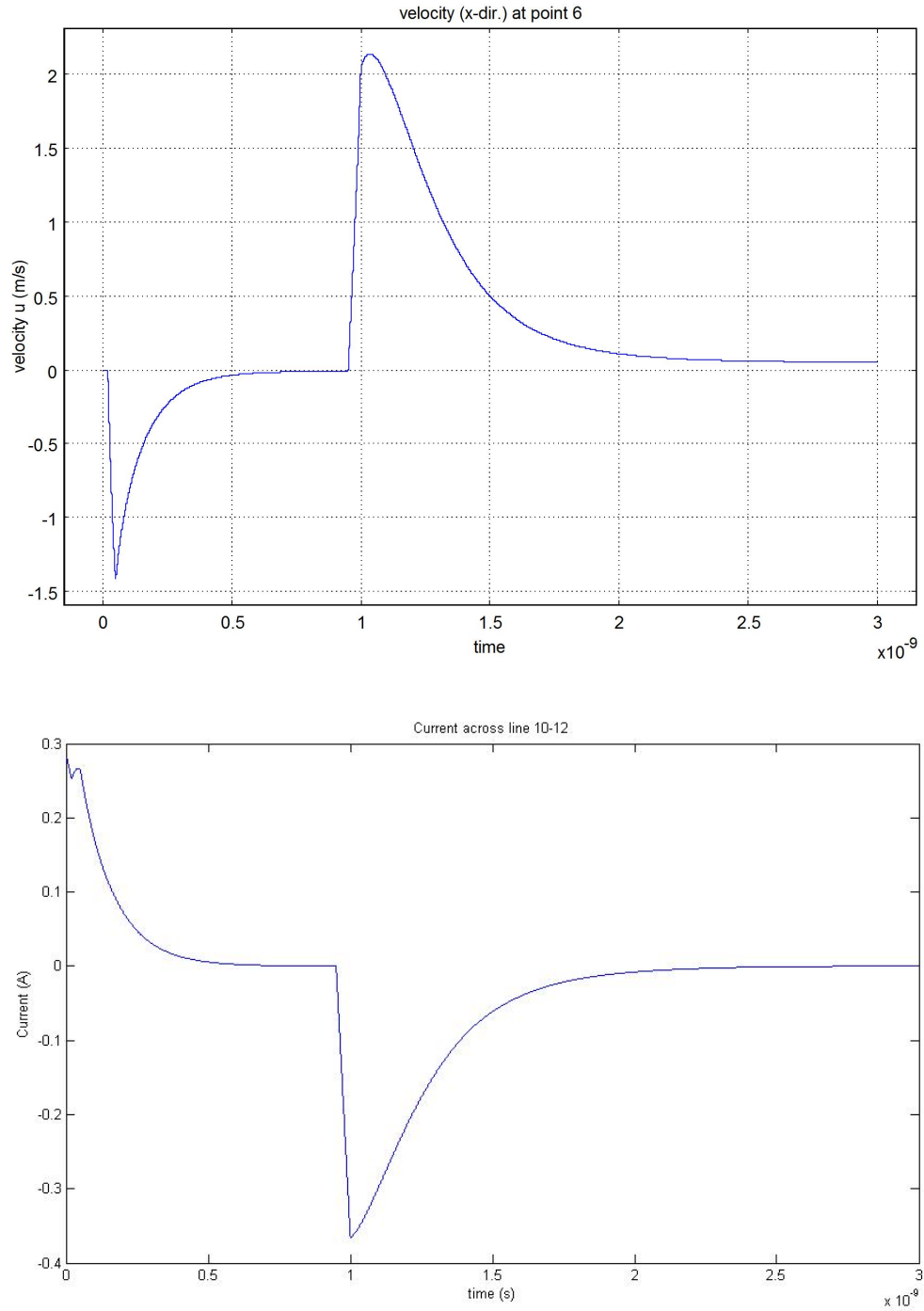
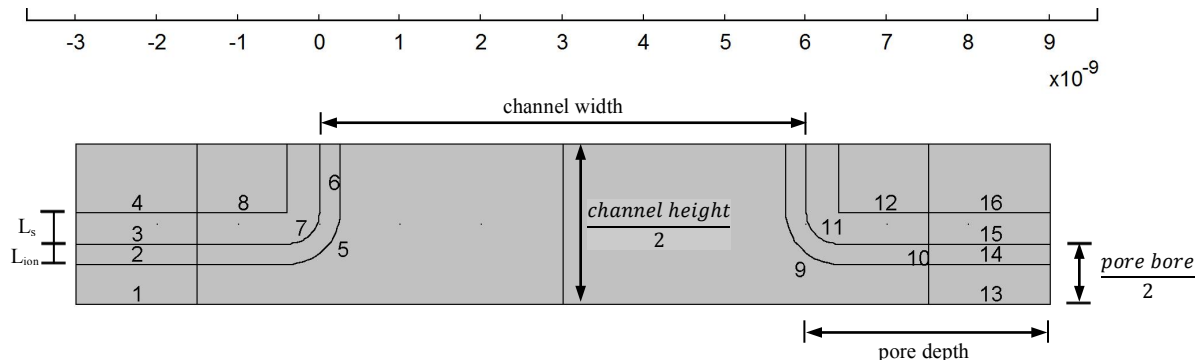


Figure 3.4: Fluid velocity (x-component) and current (x-component) as a function of time, showing equilibrium condition prior to 1 ns, and a second equilibrium condition in the latter part of Phase 2 leading up to the end of the simulation, indicating that the EDL has been fully charged

3.3.2 Geometry Parameters

The standard geometry used in the simulations is shown below in Figure 3.5 with definitions and control values for the various measurements or size parameters indicated. These values were used for all simulations in which the geometry was held constant and variations of other parameters were being studied. For simulations in which the values of geometric parameter values were studied, these were varied as discussed below in the Data and Results chapter.



parameter	description	value
pore depth	distance from pore opening to closed end of pore	3 nm
pore bore	vertical distance across pore, from top to bottom, through which ions (positive or negative) can move (does not include the Stern Layer gap); only half the total pore bore appears in the COMSOL geometry due to the symmetry	1.5 nm
channel width	horizontal distance across channel	6 nm
channel height	vertical distance across channel, from top to bottom; only half the total channel height appears in the COMSOL geometry due to the symmetry	4 nm
L _s	size of Stern Layer (thin low-permittivity gap between ion domain and electrode surface)	0.4 nm
L _{ion}	gap between edge of positive ion domain and edge of negative ion domain; amount by which positive ions can move closer to electrode surface than negative ions	0.25 nm

Figure 3.5: Standard control geometry with parameter definitions and values indicated

3.3.3 Solvent Viscosity

For the solvent viscosity, the standard control value used was one-tenth that of water, or $1/10$ of $8.9 \times 10^{-4} \text{ Pa}\cdot\text{s}$. Values on this order are justified on several physical grounds. Recent research indicates that fluids behave as if their viscosity has been reduced by 50% to 90% when subject to a strong shearing motion within a tightly-confined channel [10][21][41]. The shearing effect can be seen in Figure 3.5, which shows the x-component of the fluid velocity along a cross-section of the electrode pore.

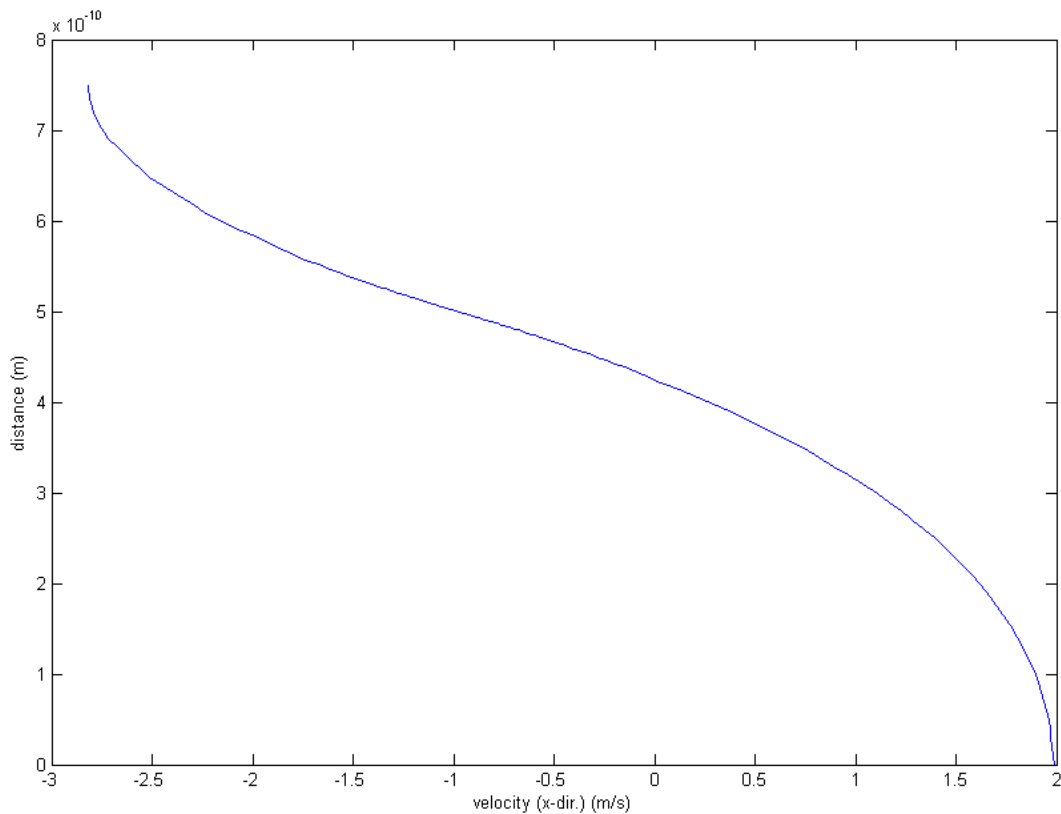


Figure 3.6: Fluid velocity (x-component) across the pore cross-section showing strong shearing effect

In the particular simulation from which this data were taken, the pore bore was 1.5 nm; Figure 3.6 plots the velocity along the upper half of the pore used in the COMSOL

geometry implementation, extending from the axis of symmetry up to the edge of the electrode, hence the 0.75 nm domain of the curve. By reflecting this velocity distribution over the axis of symmetry to account for the fluid motion in the bottom half of the pore, a wavelike curve is obtained which can be considered to have a wavelength equal to the pore bore (1.5 nm in this example). When this wavelength is on the order of the fluid's viscosity kernel (a measure of the range over which the viscosity is determined by nonlocal effects), the fluid's constitutive relation becomes nonlocal, violating one of the assumptions used in the formulation of the Navier-Stokes Equations [41]. Similar results have been shown for the viscosity of an ionic liquid [21][45]. One solution to this anomaly is to substitute a lower value for the fluid's viscosity, which will allow the Navier-Stokes Equations to be used to give an accurate qualitative description of the flow [41][42]. This approach shows agrees well with results obtained from molecular dynamics simulations in this regime.[8]

The reduced viscosity value also closely approximates the viscosity characteristics of acetonitrile (ACN), a widely used organic solvent in electrochemical systems [17].

3.3.4 Ion Mobility

For the ion mobilities, the standard control value used was one-third of the mobility in aqueous solution of the sodium (Na^+) ion, or $1/3$ of $7.877 \times 10^{-13} \text{ s} \cdot \text{mol/kg}$. As with the solvent viscosity discussed above, the electrokinetic mobility of ions has been

demonstrated to decrease from the reported, bulk-solution values when the ions are moving within tightly confined nanochannels [5][34].

For all simulations, the positive and negative ions were given identical mobilities. For simulations in which another parameter was being studied, the control value used for the ion mobility was 1/3 of $7.877 \times 10^{-13} \text{ s} \cdot \text{mol/kg}$. In one set of simulations, different values for the ion mobility were investigated and shown to have a significant effect on the charging kinetics, particularly on the contribution made by the convective current due to bulk fluid motion. These effects will be discussed fully in the Data and Results chapter below.

A word is in order regarding the units of mobility used in COMSOL. In electrochemistry, the ion mobility is defined as the ratio of a particle's terminal drift velocity to the electric field strength [5]. Therefore, mobility is usually given in the following units:

$$\frac{m/s}{V/m} = \frac{m^2}{V \cdot s}$$

If we break down Volts into its basic units, this becomes:

$$\frac{m^2}{V \cdot s} = \frac{m^2}{J/C \cdot s} = \frac{C \cdot m^2}{kg \cdot m^2/s^2 \cdot s} = \frac{s \cdot C}{kg}$$

COMSOL automatically includes Faraday's Constant F , which is C/mol , in each term of the Nernst-Planck Equation. Thus, the mobilities provided to COMSOL must be given in units that have been divided by F to compensate for this factor already being included in

the equation that COMSOL is solving. This means that, instead of $\frac{s \cdot C}{kg}$, COMSOL takes mobility in units of $\frac{s \cdot mol}{kg}$.

3.3.5 Wall Slip Condition

The fluid boundary condition at the walls is of considerable interest in the problem being investigated here due to the nanoscale dimensions. Unlike ordinary, macroscopic flows, where the ubiquitous no-slip condition is nearly always employed, nanoscale flows have been shown to behave as if the fluid is slipping over the solid wall surface to some extent [25][31][32]. In particular, at nanoscales water and other solvents have been observed to exhibit dewetting from solid surfaces, resulting in substantial fluid slip velocity at the interface.[19][30][37]

In the present investigation, the Slip Velocity option was selected in the COMSOL fluid wall boundary condition, and the magnitude of the slip was specified as a slip length. The slip length is the depth at which the fluid velocity would reach zero if the actual velocity profile were projected, to a linear approximation using its rate of change at the wall, across the wall boundary [32]. The slip length β can be expressed mathematically as follows:

$$u_{wall} = -\beta \frac{\partial u}{\partial n} \Big|_{y=0}$$

Slip lengths between 30 nm and 80 nm have been found to be realistic models of the fluid slip in nanochannels similar to the electrode pore of the present simulation [14]. Accordingly, the standard control value used for the slip length was 30 nm. Other slip

length values were also investigated, and their effects on the fluid motion and EDL charging are discussed below.

3.4 Postprocessing

3.4.1 Generation of data tables and graphs

Certain simulation results, such as ion concentration, electric potential, and velocity profiles along various segments of the geometry, were generated and plotted directly in COMSOL using the Line Graph and Surface Plot functions. Other data types, such as charge densities and current densities, were tabulated in COMSOL using the Point Evaluation and Table Plot functions to evaluate a given functional expression at each point in time. For all simulations, a time step of 0.5 ps was used. The tabular data were then saved as text files and imported into Matlab, where plots were generated that allowed comparison of data sets from different simulations to show the effects of parameter variation on the charging performance indicators being analyzed.

3.4.2 Electrode surface charge density

One of the most important indications of EDL charging performance in these simulations is the charge density on the electrodes, which provides a direct measure of the amount of charge that has been accumulated in the charging process. Thus, it is instructive to examine how this charge density evolves with time as the EDL charges, and to compare the charging curves from simulations with different values for one of the parameters being studied.

The electrode surface charge density was computed by integrating the spatial charge density in the EDL over a domain adjacent to the electrode surface of interest. For the analysis in the present study, the surface charge densities were assessed using the electrode pore surface, starting 1.5 nm from the mouth of the pore and extending to the closed end of the pore. This surface, and the adjacent electrolyte volume over which the charge density integration was performed (domain regions 1 and 2), are highlighted in Figure 3.7.

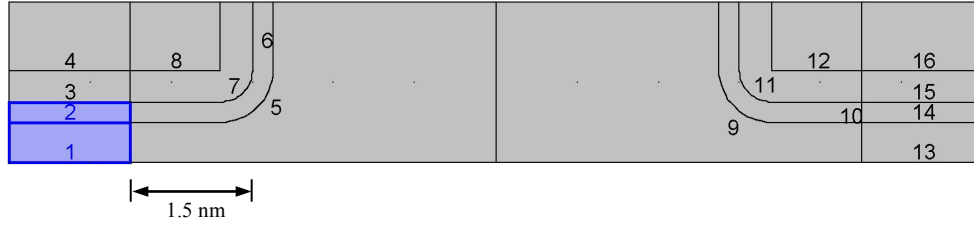


Figure 3.7: Integration of electrolyte spatial charge density to compute electrode surface charge density on adjacent electrode surface

Because the geometry model incorporates the axial symmetry condition and thus models half the pore volume, the integrated spatial charge density will be equal to (and have the opposite polarity of) the charge on half the pore surface, or the entire upper bounding surface that appears in Figure 3.7. Therefore, the surface charge density (per unit of depth in the z-direction) is given by:

$$\sigma_e = \iint_A \frac{(c_+ - c_-) \cdot F}{(pore\ depth - 1.5\ nm)} dA$$

The electrode pore surface charge density σ_e was computed for each time step and plotted as a function of time for each simulation. The charge density curves were compared for different simulations to reveal the effect of variations in simulation parameters on the EDL charging rate.

3.4.3 Charging current and current density

To calculate the current density at a point within the electrolyte, we recall the Nernst-Planck Equation:

$$\vec{J}_i = c_i z_i \vec{v}_i F - D_i z_i \vec{\nabla} c_i \cdot F$$

where the ion velocity \vec{v}_i is given by

$$\vec{v}_i = \vec{u} + (-\vec{\nabla}\phi) z_i \mu_i F$$

These two relations, taken together, provide the current density \vec{J}_i for species i at a point.

In the model of interest in the present study, there are two species present: the positive ions, which have a charge of $+e$, and the negative ions, which have a charge of $-e$.

Therefore, we can express the positive ion current density as

$$\vec{J}_+ = c_+ F^2 \mu_+ (-\vec{\nabla}\phi) - D_+ F \vec{\nabla} c_+ + c_+ F \vec{u}$$

and the negative ion current density as

$$\vec{J}_- = c_- F^2 \mu_- (-\vec{\nabla}\phi) - D_- F \vec{\nabla} c_- + c_- F \vec{u}$$

Combining these two current densities using the principle of superposition, and making use of our condition that both ion species have the same mobility and diffusion coefficients ($\mu_+ = \mu_-$ and $D_+ = D_-$), we obtain the expression for the total current density:

$$\vec{J}_{tot} = (c_+ + c_-)F^2\mu(-\vec{\nabla}\phi) - DF(\vec{\nabla}c_+ - \vec{\nabla}c_-) + (c_+ - c_-)F\vec{u}$$

This expression reveals the three sources of ion motion under the model being studied: the first term represents ion migration due to the electric field, the second term represents diffusion, and the third term (the convective term) represents ion transport due to bulk fluid motion. Thus, we can calculate the current density due to convection using the convective term only:

$$\vec{J}_{conv} = (c_+ - c_-)F\vec{u}$$

The difference $\vec{J}_{tot} - \vec{J}_{conv}$ gives the current density due to ion migration and diffusion. These are the two transport phenomena that are modeled using a standard PNP model and which have been studied extensively in prior simulations of EDL charging kinetics. Therefore, one primary goal of the present investigation is to compare the current and current densities given by the standard PNP model (migration and diffusion) to those realized when the convective term is added, thus revealing the degree of impact made by the addition of the convective transport to the model.

In this study, the current density in the x-direction was evaluated as a function of position along a cross-section of the pore. The cross-section used for these evaluations (line segments 10 and 12) is shown in Figure 3.8.

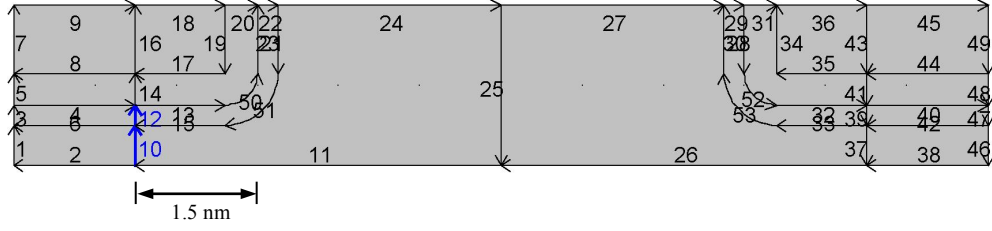


Figure 3.8: Electrode pore cross-section used to evaluate current density

The current densities were evaluated in the x-direction, taking the x-components of the above formulas:

$$J_{x,tot} = (c_+ + c_-)F^2\mu\left(-\frac{\partial\phi}{\partial x}\right) - DF\left(\frac{\partial c_+}{\partial x} - \frac{\partial c_-}{\partial x}\right) + (c_+ - c_-)Fu_x$$

$$J_{x,conv} = (c_+ - c_-)Fu_x$$

The current density J_x was plotted as a function of position on the cross-section at various times during the charging process to give snapshots of the charging kinetics. These current evaluations will be discussed more fully below in the Data and Results chapter.

The current (per unit depth in the z-direction) across the cross-section shown in Figure 3.8 was computed by integrating the current density J_x along the line:

$$I_x = \int_C J_x ds$$

The current was plotted as a function of time to reveal how the current flowing into the pore evolves over time as the EDL charges. These charging current curves were compared for different simulations to investigate the effect of different simulation parameter values on the charging current.

CHAPTER 4

RESULTS AND DISCUSSION

4.1 Illustration of the fluid and ion dynamics in the pore and channel system

To give the reader a feel for the problem, and to enhance understanding of the results and comparisons that follow, we first present a set of simulation results showing how the ion concentrations, electric potential, and fluid velocity evolve with time as the simulation progresses. For this demonstration, all the standard control values for the parameters were used: 1/10 viscosity, 30 nm slip length, 1/3 mobility, 1.5 nm pore bore, and 3 nm pore depth.

To illustrate the evolution of electric potential, the potential was plotted along the axis of symmetry extending across the centerline of the pore/channel geometry from the negative pore, through the channel, to the positive pore, as shown in Figure 4.1. Figure 4.2 shows the potential along this axis plotted at various times during the charging process.

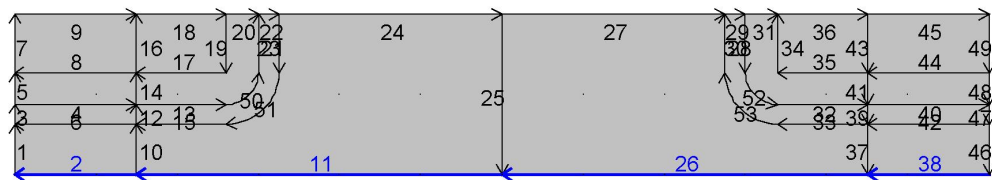


Figure 4.1: Axis of symmetry along which electric potential was plotted

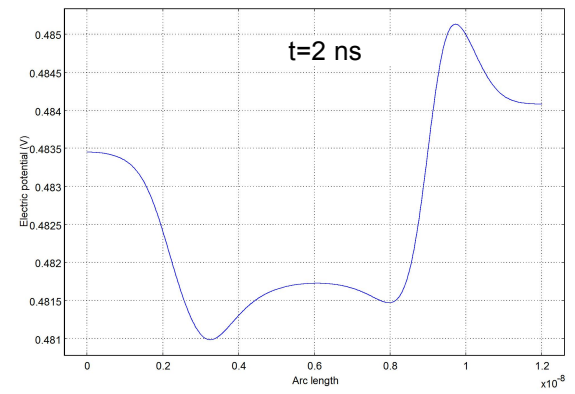
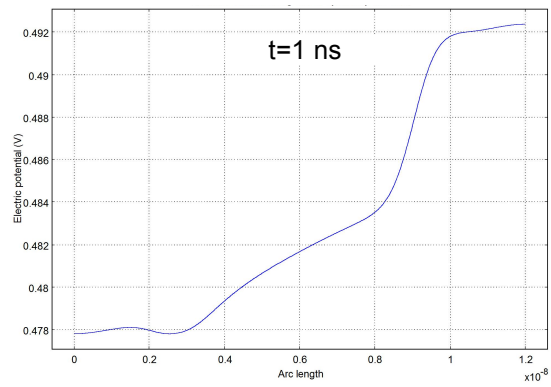
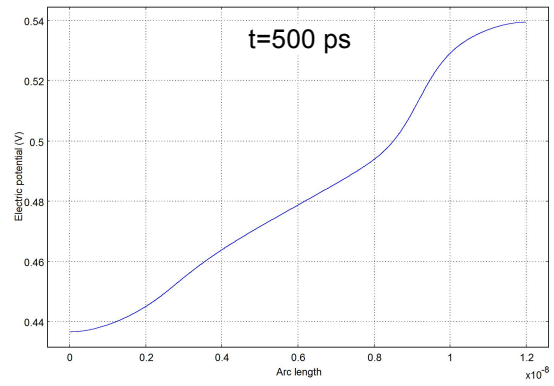
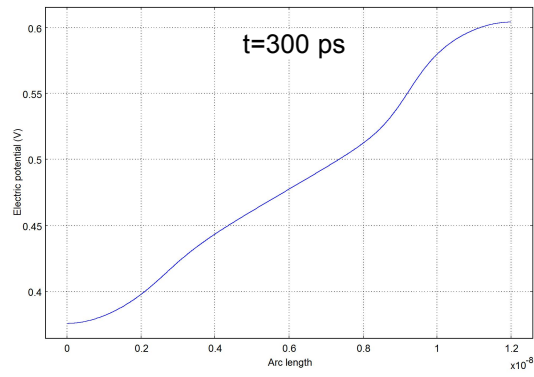
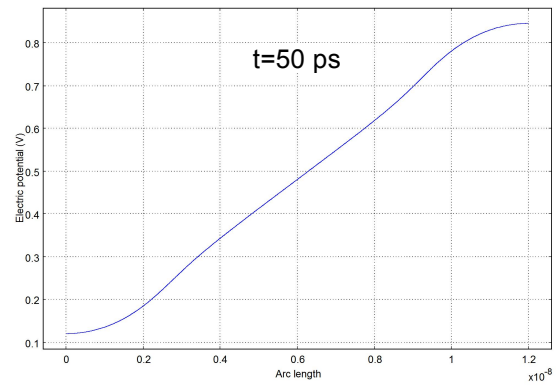
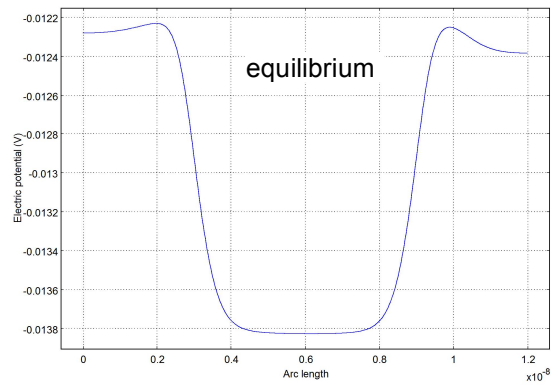


Figure 4.2: Electric Potential along axis of symmetry

As we can see, at equilibrium before charging begins, the potential starts off slightly negative along the entire axis. This is caused by the fact that there is an equal number of positive and negative ions in the overall fluid domain, and there is a portion of the domain adjacent to the electrode surfaces (see Figures 3.2(d) and (e)) that is accessible only to positive ions. Some positive ions will migrate into this region, leaving a slight excess of negative charge in the remainder of the fluid domain. The equilibrium potential is slightly higher (but still negative) inside the pores, where the symmetry axis along which the plots of Figure 4.2 were made is closer to the accumulation of positive charge near the electrode surfaces.

As the applied potential is turned on across the electrodes, a potential difference rapidly develops along the axis of symmetry as shown in the second plot of Figure 4.2, which was taken 50 ps after the start of charging. In these early stages of the charging, the potential difference is nearly the full 1 V potential that is applied across the electrodes. As the charging continues, counterions accumulate adjacent to each electrode as the EDL develops, screening off the charge on the electrode itself and reducing the potential difference within the bulk electrolyte. Thus, 500 ps into the charging, the potential difference between the left and right ends of the symmetry axis is only 0.1 V, and by 1 ns it is less than 0.02 V. The majority of the 1 V potential difference between the two electrodes occurs in the Stern Layer low-permittivity gaps immediately surrounding the electrode surface and which are inaccessible to ions.

A different view of this same evolution process is seen in Figure 4.3, which plots the concentrations of both ion species at various times throughout the charging process.

These concentration plots were made along the same axis of symmetry as the potential plots just discussed, and the label c_3 represents the positive ion concentration, while the label c_4 represents the negative ion concentration.

At equilibrium, negative ion concentration is slightly higher than positive ion concentration inside the pores, and this is due to some of the positive ions migrating into the narrow region along the electrode surface, further away from the line of symmetry where these plots were made. Out in the channel, away from the electrodes, both ion species have equal concentrations.

As the electric potential is applied across the electrodes and the EDLs begin to develop, the difference between c_3 (positive ion concentration) and c_4 (negative ion concentration) grows, as revealed by the scale on the vertical axis of the plots. Negative ion concentration spikes at the right end, which is inside the positive electrode pore. At the left side of the plots (inside the negative electrode pore), negative ion concentration falls, as expected. The positive ion concentration, however, does not show a concomitant spike on this side; this is because the dense concentration of positive ions forming the EDL is located in the thin domain gap accessible only to positive ions adjacent to the electrode surface, above the axis of symmetry.

Figure 4.4 shows an arrow plot of the fluid velocity throughout the pore-and-channel fluid domain at 1 ns, revealing the strong shearing effect discussed above in Chapter 3. Figure 4.5 shows how the magnitude of the fluid velocities varies as the ions reach equilibrium in the first 1 ns and then charge the EDL between 1 ns and 3 ns. This

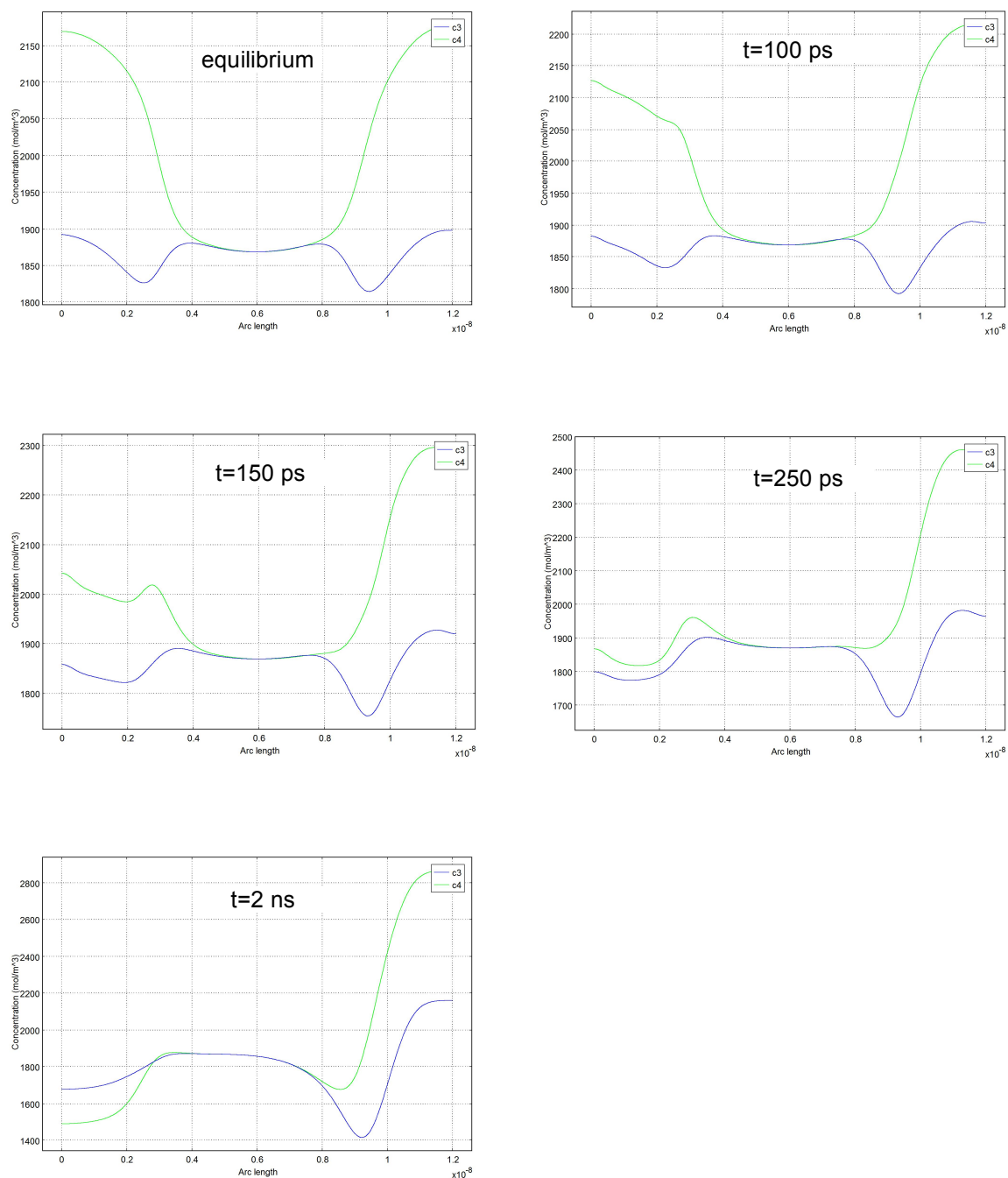


Figure 4.3: Ion concentrations along axis of symmetry

plot of velocity as a function of time was made at the point as indicated, which is located along the axis of symmetry inside the negative electrode pore.

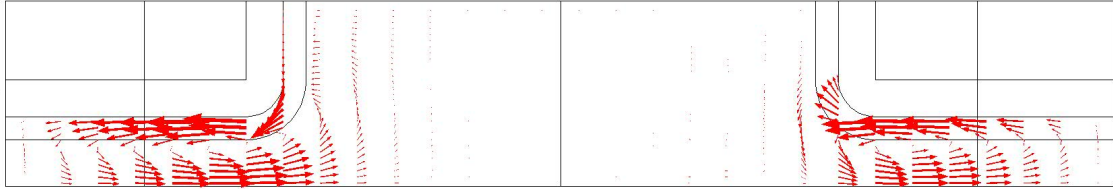


Figure 4.4: Fluid velocity field throughout the channel/pore domain at $t=1$

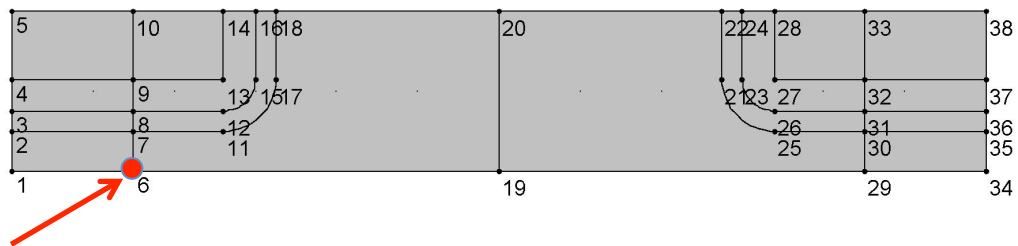
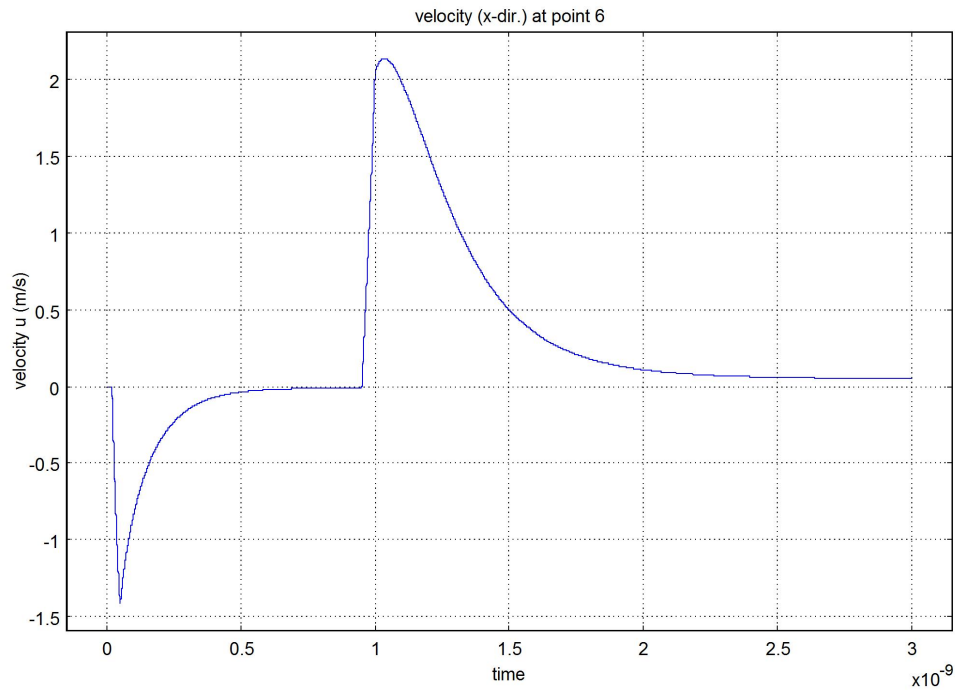


Figure 4.5: Fluid velocity (x-component) across the pore cross-section

4.2 Demonstration of the convective charging current effect

Consider the first two simulations that follow. This set used all the standard control values as stated above for the parameters:

	sim #1	sim #2
solvent viscosity	1/10	no flow
wall slip length	30 nm	no flow
ion mobility	1/3	1/3
pore bore	1.5 nm	1.5 nm
pore depth	3 nm	3 nm

For simulation #1, which included the flow modeling, the solvent viscosity was 1/10 that of water, and the ion mobility in each simulation was 1/3 of the standard mobility of the sodium (Na^+) ion, or $1/3$ of $7.877 \times 10^{-13} \text{ s} \cdot \text{mol/kg}$.

The only difference between these two simulations was that the first simulation included the Navier-Stokes bulk fluid flow modeling, while the second one did not. This comparison thus provides a good starting point from which to evaluate the effect of flow modeling on the EDL charging process.

To facilitate comparison, we plot the electrode charge density curves as a function of time throughout the EDL charging process for these two simulations. These curves are shown in Figure 4.6. In this plot, time $t=0$ is the start of the charging process, the moment when the electric potential is applied across the electrodes. The ion distribution in the electrolyte solution was allowed to reach equilibrium prior to the start of charging, as

discussed in Chapter 3, but this part of the simulation is not shown in the figures presented in this chapter.

In Figure 4.6, we see that charge accumulates in the EDL slightly faster in the simulation with flow modeling as compared to the simulation without flow modeling.

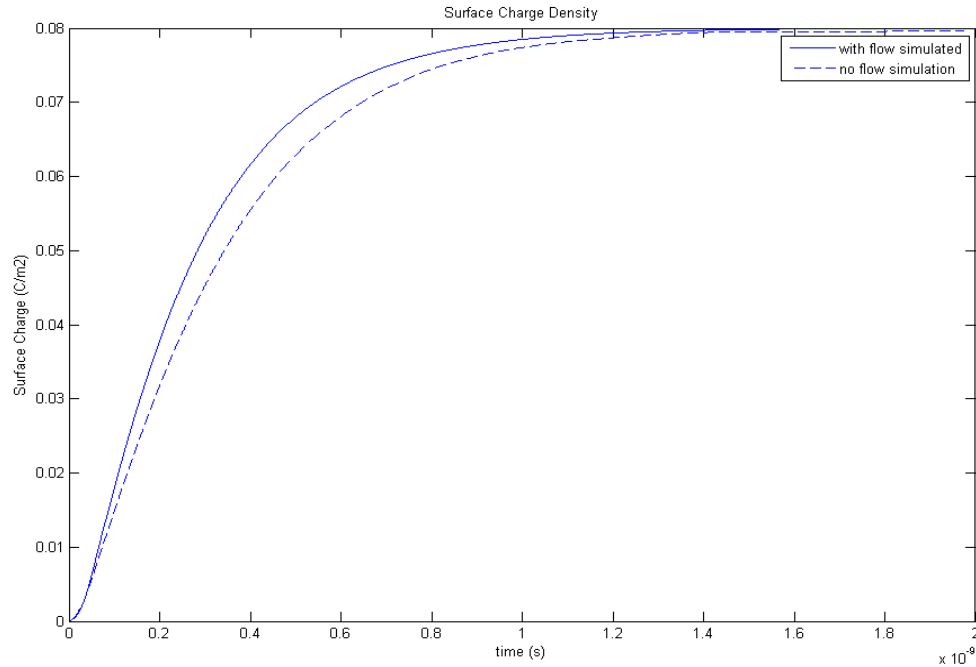


Figure 4.6: Comparison of electrode charge density curve for simulations with and without flow simulation using standard control parameter values

One useful way to quantify the difference in charging times is to measure how much time each simulation requires to reach a specified percentage of the steady-state, fully-charged level. In the case shown in Figure 4.6, the simulation including flow modeling reached 90% of the steady-state charge density (0.08 C/m^2) in 598 ps, compared to 706 ps without flow simulation. This represents a 15 percent shorter time required to achieve this charge level when the charging is aided by the convective current.

Another useful way of quantifying the difference in charging times is to compute a time constant for each simulation. The time constant is based on the fact that the charge accumulates according to a decaying exponential function of time:

$$Q(t) = Q_{\infty} \left(1 - e^{-\frac{t}{\tau}}\right)$$

where Q_{∞} is the steady-state, equilibrium charge level. By rearranging this equation and taking the natural logarithm of both sides, we obtain

$$\ln \left(1 - \frac{Q}{Q_{\infty}}\right) = -\frac{t}{\tau}$$

This quantity is linear in time, and the slope is the negative reciprocal of the time constant, τ . For the two simulations discussed in this subsection, the charging factor plots, along with linear curve fits and time constants, are shown in Figure 4.7.

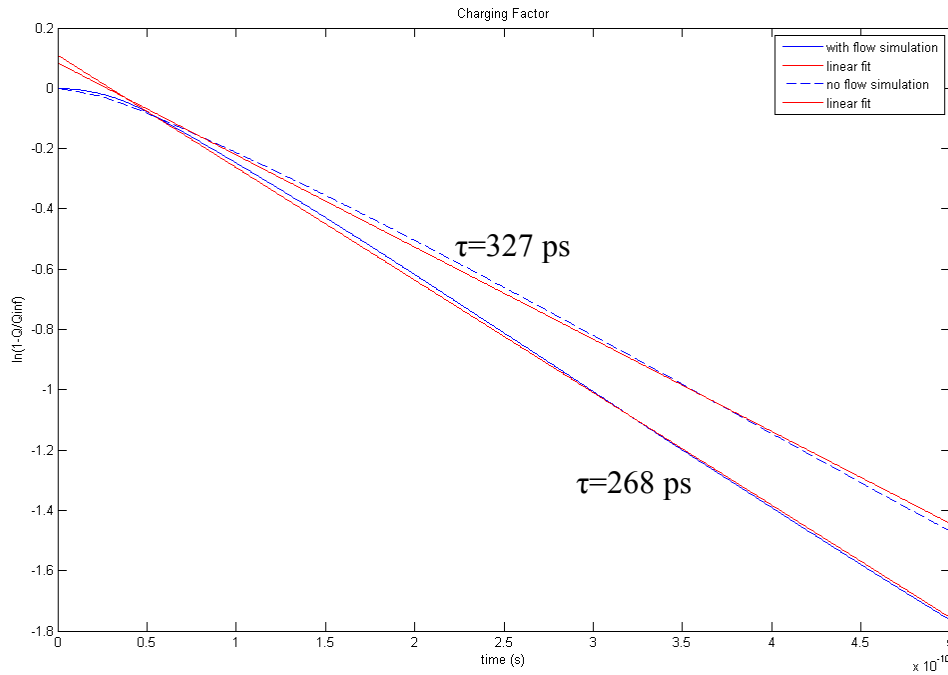


Figure 4.7: Log plot of charging factor revealing time constants

The more rapid accumulation of charge in the simulation with flow modeling suggests that levels are higher in that simulation. This is indeed revealed in the plot charging current in the electrode pore, shown in Figure 4.8. Here, we see that the current

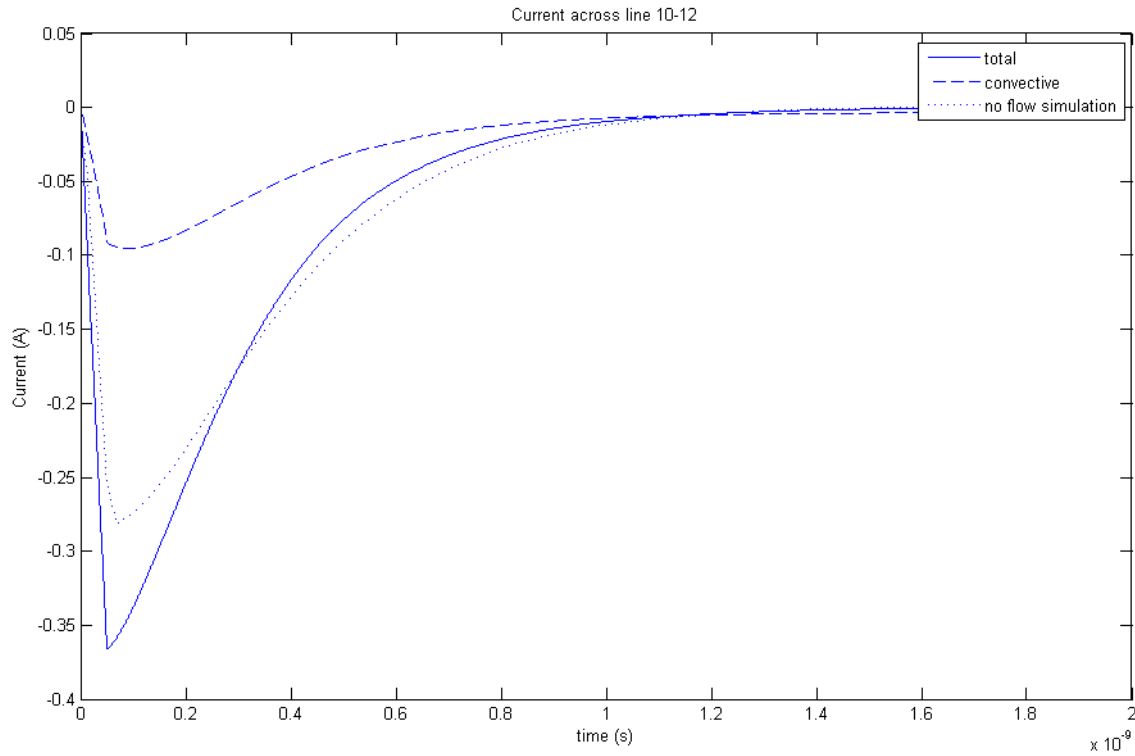


Figure 4.8: Comparison of charging current curve for simulations with and without flow simulation using standard control parameter values

in the simulation with flow modeling (solid line) is appreciably greater than the current in the simulation without flow simulation (dotted line), and the convection term (dashed line) appears to account for most of the difference. This presents evidence that bulk fluid motion in the electrolyte solution will carry ions with it at such a rate as to increase the total charging current and, in turn, speed up the EDL charging process.

4.3 Effect of varying the solvent viscosity

In the next series of simulations, the solvent viscosity was varied while keeping all other simulation parameters unchanged.

	sim #1	sim #2	sim #3	sim #4
solvent viscosity	1/10	1/3	actual-water	no flow
wall slip length	30 nm	30 nm	30 nm	no flow
ion mobility	1/3	1/3	1/3	1/3
pore bore	1.5 nm	1.5 nm	1.5 nm	1.5 nm
pore depth	3 nm	3 nm	3 nm	3 nm

Here, we have three simulations that were run with different solvent viscosity values, and one simulation that was run with no flow modeling, making solvent viscosity irrelevant in that one. The solvent viscosity values are specified relative to the standard viscosity of water.

For this set of four simulations, we once again plot the electrode surface charge density as a function of time throughout the charging process and superimpose the curves to facilitate comparison of the charging rates. This comparison is shown in Figure 4.9.

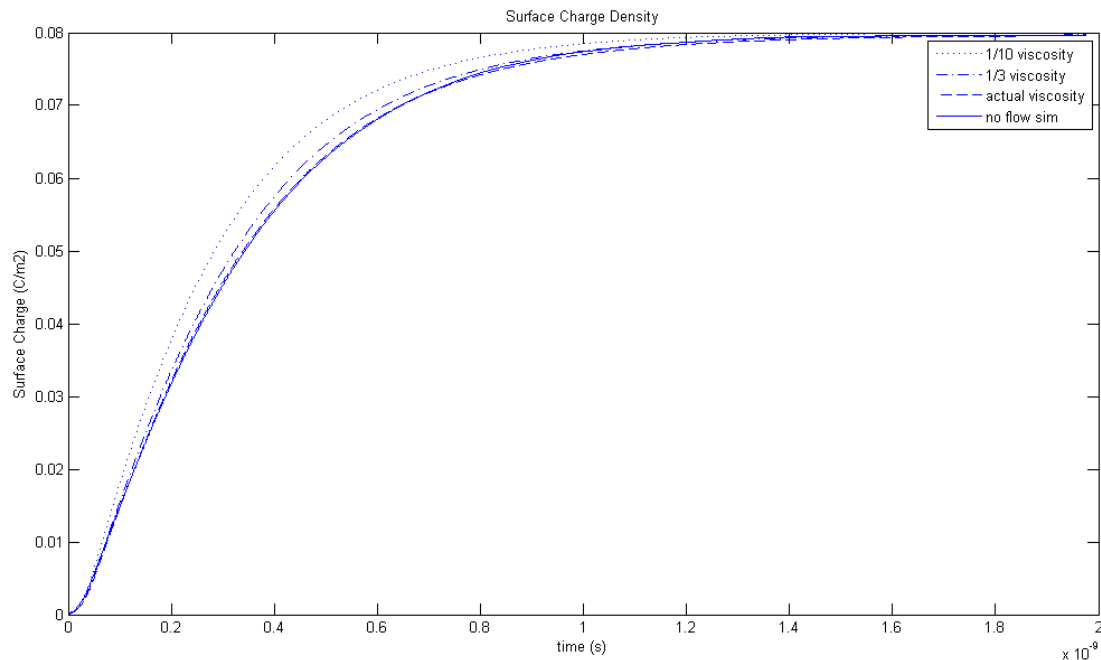


Figure 4.9: Comparison of electrode charge density curves for simulations with different solvent viscosities

This figure shows the critical impact of solvent viscosity on the convective charging effect. With a solvent having a viscosity equal to the actual viscosity of water, the EDL charging curve is practically indistinguishable from that of the no-flow simulation. This congruence suggests that the charging current due to convection is minuscule at this viscosity level. When solvent viscosity is reduced to 1/3 of water's viscosity, the gap is small but noticeable. At 1/10 of water's viscosity, the EDL charges noticeably faster than in the no-flow case; this is the same data set that was presented in the first set of simulations above.

This effect of solvent viscosity on the EDL charging rate, and its apparent origin in the convective current, can be verified by examining the convective component of the charging current in the different simulations.

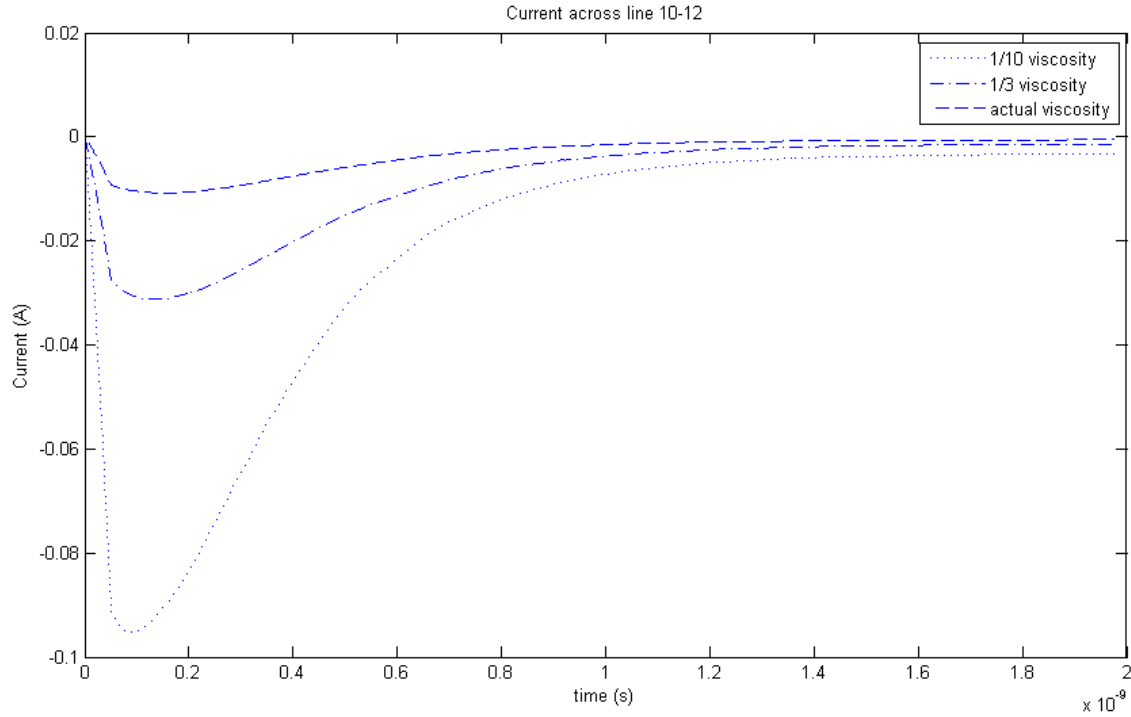


Figure 4.10: Comparison of convective component of the pore current for simulations with different solvent viscosities

The convective current curves, shown in Figure 4.10, show that the magnitude of the convective component of the charging current within the electrode pore is much smaller for the 1/3 viscosity simulation compared to the 1/10 viscosity simulation. The peak convective current for the 1/10 viscosity case is 0.0953 A, compared to 0.0312 A for the 1/3 viscosity case, representing a factor of slightly greater than 3. The convective current in the simulation with actual viscosity of water peaks 0.0108 A, nearly 9 times less than in the 1/10 viscosity case. The origin of this effect can be verified by examining the bulk

fluid velocities along the same cross-section of the electrode pore where the current measurements were taken.

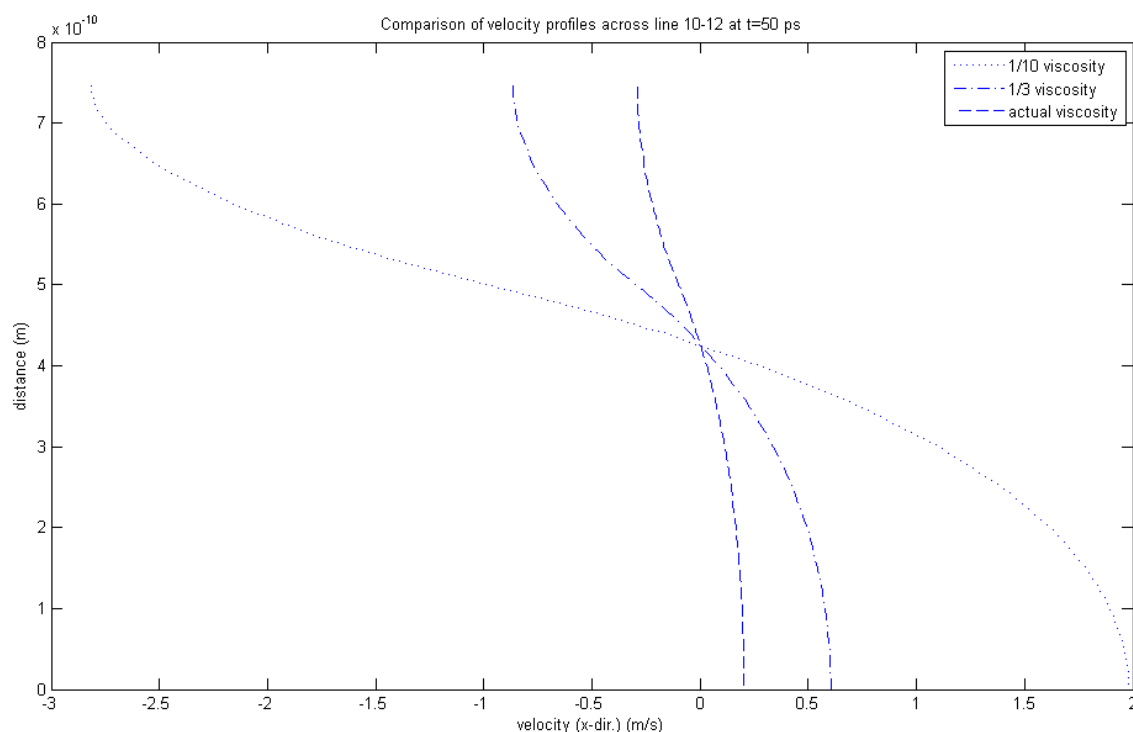


Figure 4.11: Comparison of fluid velocity profile along pore cross-section at $t=50$ ps for simulations with different solvent viscosities

The velocity profiles shown in Figure 4.11 were taken at 50 ps after the start of charging, and all three simulations in this group show their peak current near this time (by reference to the convective current curves in Figure 4.4). At this time, the maximum velocity in the 1/10 viscosity case is 2.82 m/s, compared to 0.87 m/s for the 1/3 viscosity case, representing a factor of 3.2. The velocity in the simulation with actual viscosity of

water reaches a maximum of 0.29 m/s, nearly 10 times less than in the 1/10 viscosity case.

From these comparisons, we can conclude that the magnitude of the velocities seen in the bulk fluid flow field is a primary factor that determines the amount of electric current due to ion advection. Because viscosity has a direct impact on the velocities in a flow field, it is directly correlated with the convective current seen in the EDL charging process.

4.4 Effect of varying the wall slip length

In the next series of simulations, the wall slip length was varied while keeping all other simulation parameters unchanged.

	sim #1	sim #2	sim #3	sim #4
solvent viscosity	1/10	1/10	1/10	no flow
wall slip length	0	30 nm	50 nm	no flow
ion mobility	1/3	1/3	1/3	1/3
pore bore	1.5 nm	1.5 nm	1.5 nm	1.5 nm
pore depth	3 nm	3 nm	3 nm	3 nm

Here, we have three simulations that were run with different wall slip length values, and one simulation that was run with no flow modeling, making the fluid slip irrelevant in

that one. The fluid material properties, such as solvent viscosity, were identical in all four simulations in this group.

For this set of four simulations, we once again plot the electrode surface charge density as a function of time throughout the charging process and superimpose the curves to facilitate comparison of the charging rates. This comparison is shown in Figure 4.12.

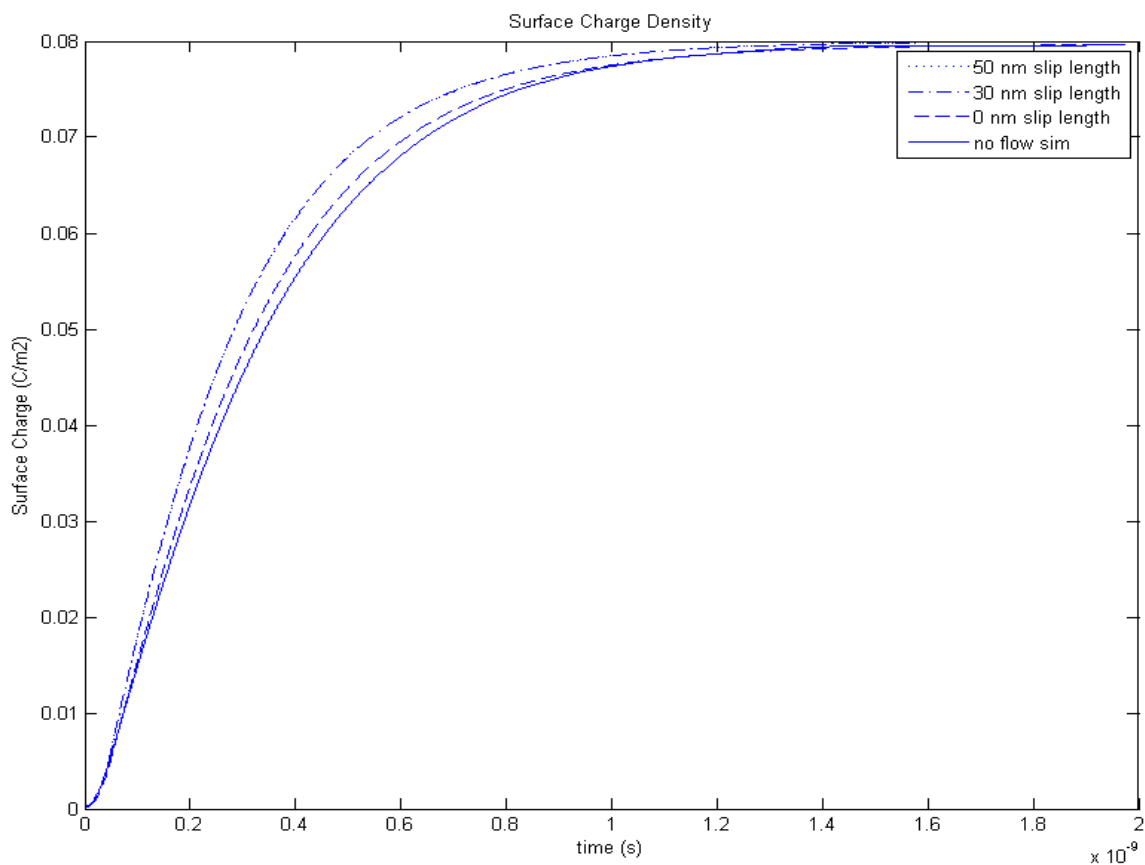


Figure 4.12: Comparison of electrode charge density curves for simulations with different wall slip lengths

In Figure 4.12, the curves for the 30 nm and 50 nm slip lengths are indistinguishable. This is expected because the lower wall friction levels accompanying the higher slip

lengths are negligibly small when compared to the unchanging friction within the fluid itself due to the strong shear seen in the velocity profile (Figure 3.6). Once the wall friction becomes sufficiently small, any further reduction is indistinguishable from the friction within the fluid, which dominates.

An additional explanation for the invariance between the 30 nm and 50 nm slip length cases is seen by observing that the slip length is many times greater than the pore bore (1.5 nm), which means that the velocity at this distance away from the hypothetical “wall” represented by the slip length is essentially unchanging, as seen by the velocity curves being nearly perpendicular to the wall. At this range of slip lengths, further increase in the slip length will not result in discernible change the fluid velocities. The 0 nm slip length case represents the standard no-slip boundary condition, and Figure 4.12 reveals that this condition appreciably slows the EDL charging compared to the simulations with large slip lengths.

We can confirm this hypothesis by examining the velocity profiles along the pore cross-section at a particular time, such as $t=50$ ps, as shown in Figure 4.13. The velocity profiles for the 30 nm and 50 nm slip lengths are indistinguishable, as posited above. The profile for the 0 nm slip length case looks quite different, exhibiting a drastic drop in velocities in the top region of the pore, which is closest to the electrode surface. This is expected and required in order to satisfy the no-slip condition, which requires that the fluid velocity fall to zero at the wall. This significantly reduces the average fluid velocity within the pore and accounts for the slower charging of the EDL in this simulation.[27]

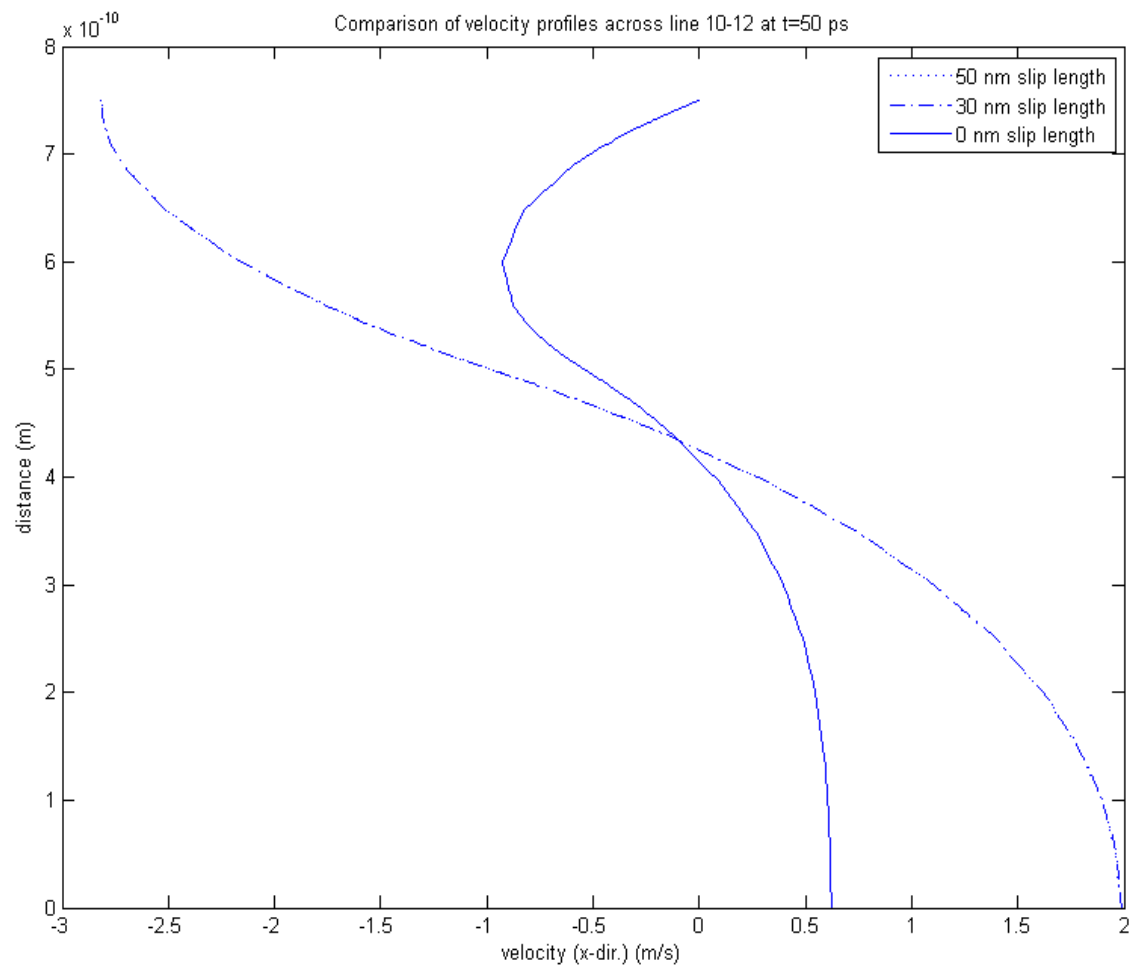


Figure 4.13: Comparison of fluid velocity profile along pore cross-section at t=50 ps for simulations with different slip lengths

Further confirmation of the slip length effect on charging rate is provided by the electric current in the pore, which is plotted in Figure 4.14. As expected, the current curves for the 30 nm and 50 nm slip length simulations are indistinguishable.

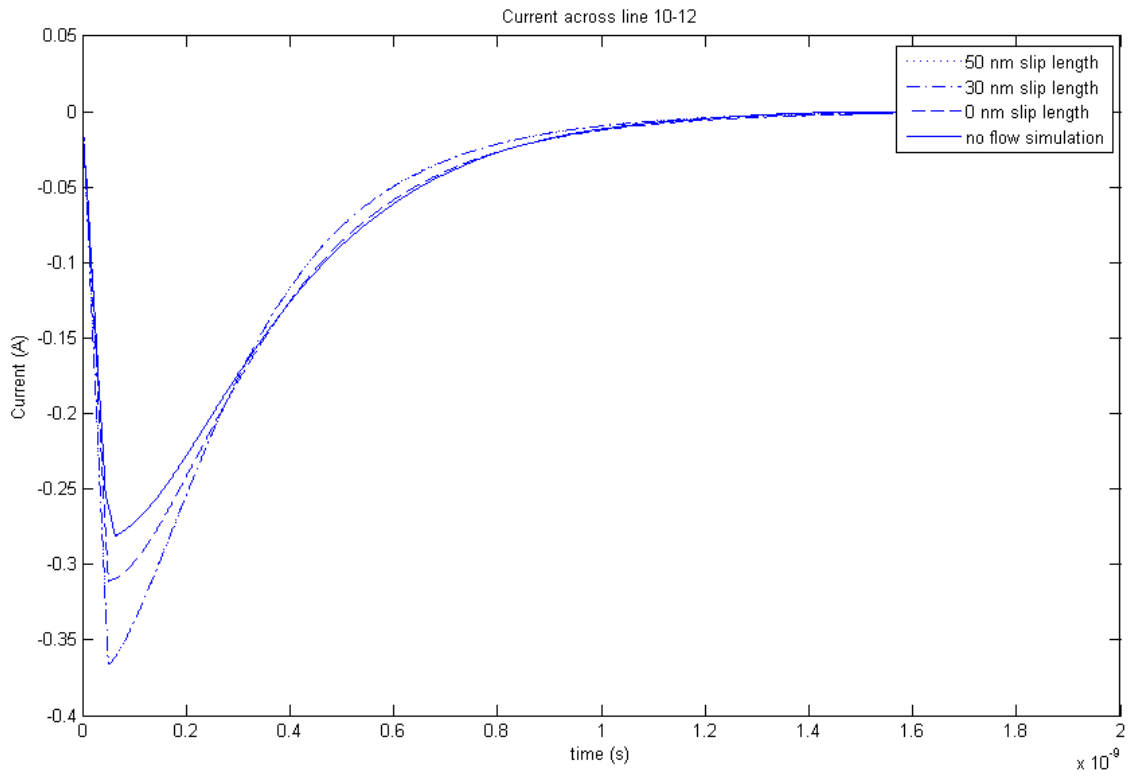


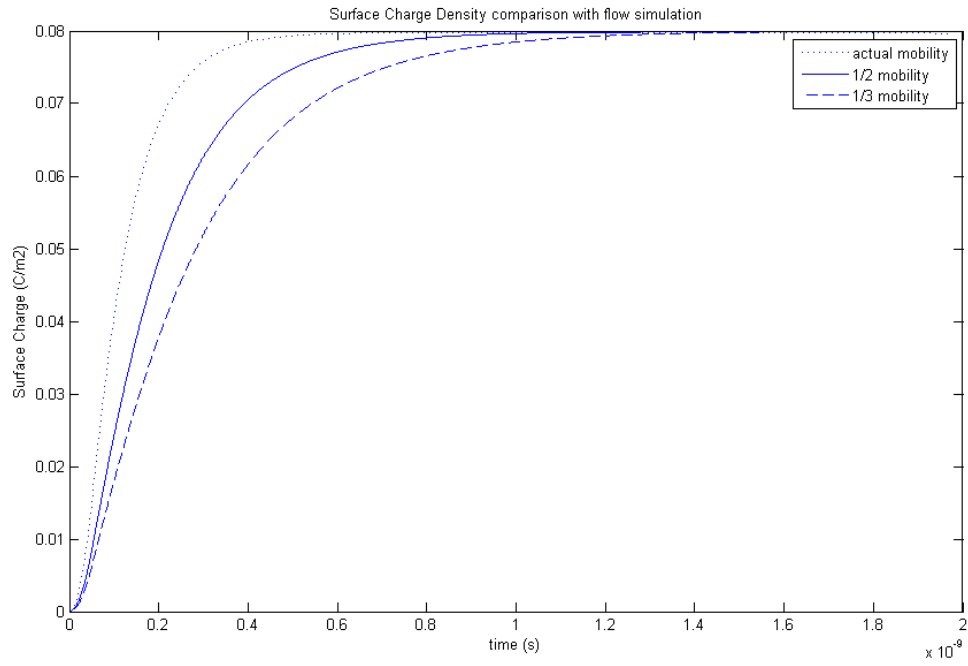
Figure 4.14: Comparison of charging current curve for simulations with different slip lengths

4.5 Effect of varying the ion mobility

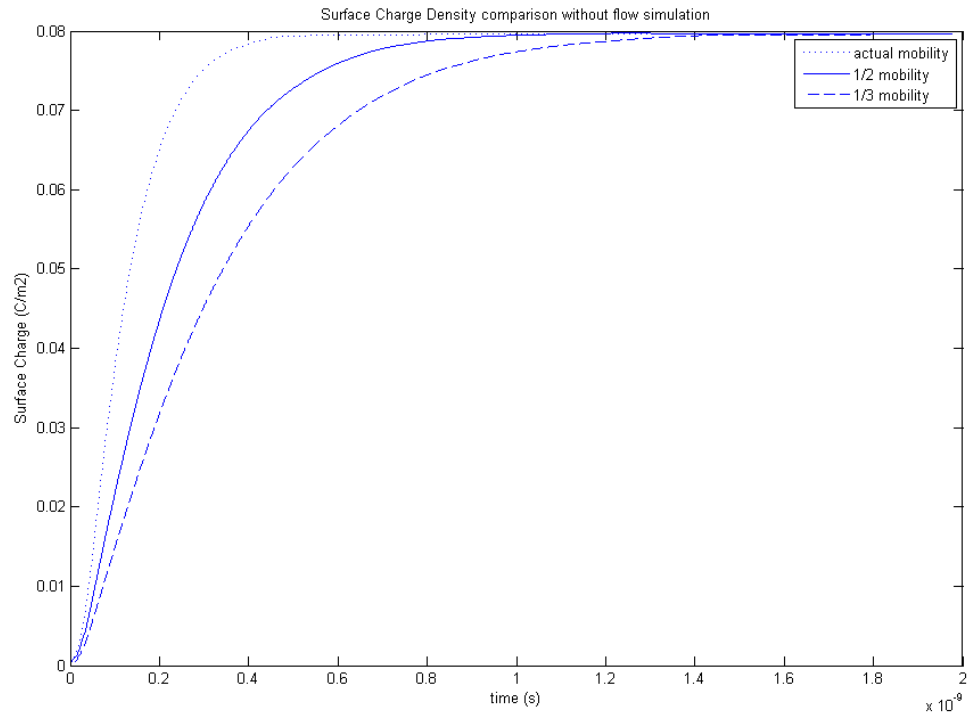
In the next series of simulations, the ion mobility was varied while keeping all other simulation parameters unchanged. Six simulations were performed in this set to allow each of three ion mobility values ($1/3$, $1/2$, and actual mobility of the Na^+ ion) to be investigated both with and without bulk flow simulation.

	sim #1	sim #2	sim #3	sim #4	sim #5	sim #6
solvent viscosity	1/10	no flow	1/10	no flow	1/10	no flow
wall slip length	30 nm	no flow	30 nm	no flow	30 nm	no flow
ion mobility	1/3	1/3	1/2	1/2	actual- Na^+	actual- Na^+
pore bore	1.5 nm	1.5 nm	1.5 nm	1.5 nm	1.5 nm	1.5 nm
pore depth	3 nm	3 nm	3 nm	3 nm	3 nm	3 nm

The electrode charge density curves for these simulations are shown in Figure 4.15. Figure 4.15(a) compares the curves for the three simulations performed with bulk flow modeling, and Figure 4.15(b) compares the curves for the three simulations performed without bulk flow modeling. Within each group, the use of greater ion mobility results in faster accumulation of charge in the EDL, as expected. Using the same metric developed above, the simulations with bulk flow modeling took 598 ps, 429 ps, and 243 ps to reach 90 percent of the steady state charge density value using ion mobilities of $1/3$, $1/2$, and actual mobility of the Na^+ ion, respectively. For the simulations without bulk flow modeling, the times required to reach 90 percent of the steady state charge value were 706 ps, 487 ps, and 261 ps, respectively.



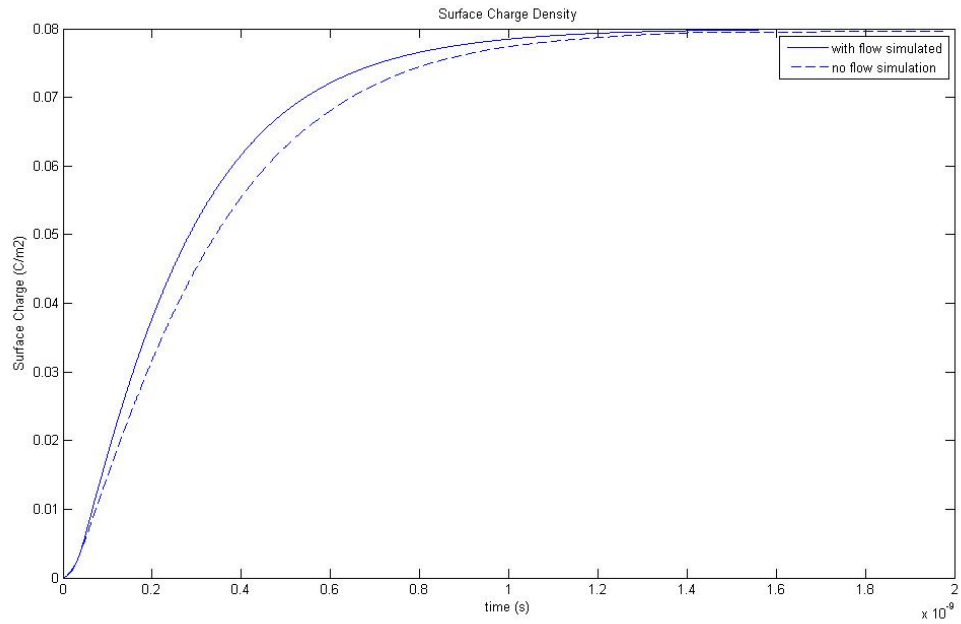
(a) with bulk flow modeling



(b) without bulk flow modeling

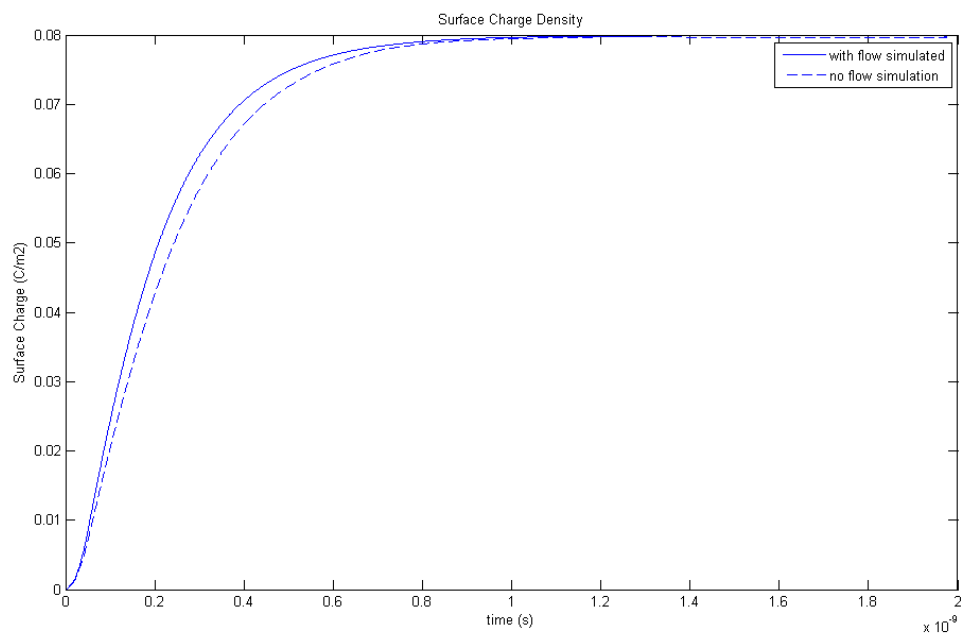
Figure 4.15: Comparison of electrode charge density curves for simulations with different ion mobilities

These charging times suggest another informative comparison: for each given value of ion mobility, comparing the charge density curve with bulk flow modeling to that without bulk flow modeling. These comparisons are illustrated in Figure 4.16(a)-(c).

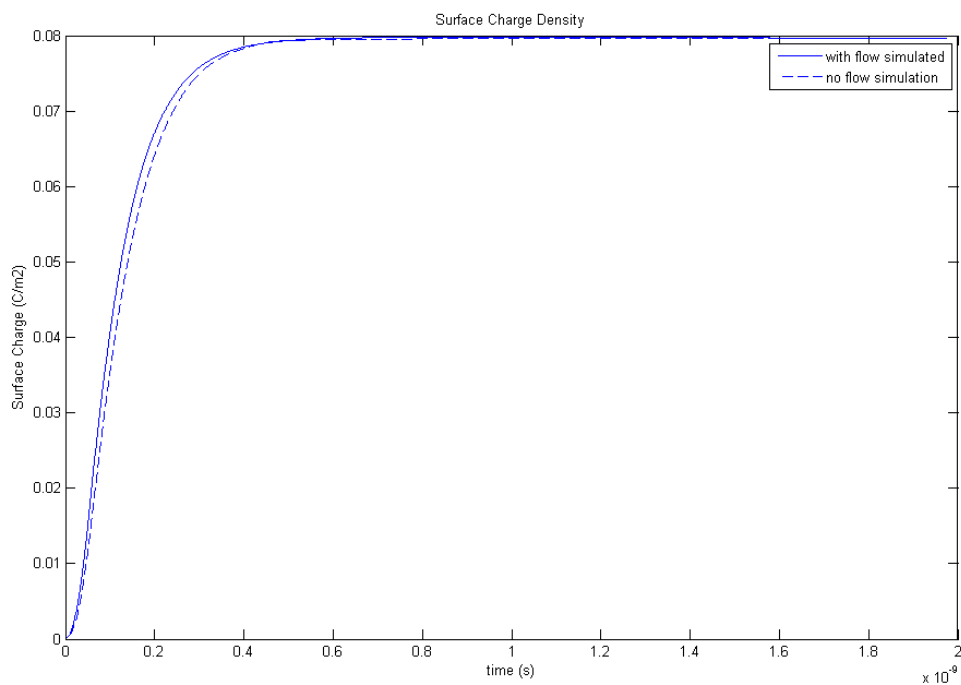


(a) 1/3 mobility

Figure 4.16: Comparison of electrode charge density curves for simulations with different ion mobilities



(b) 1/2 mobility



(c) actual Na⁺ mobility

Figure 4.16 (cont'd.): Comparison of electrode charge density curves for simulations with different ion mobilities

The comparisons illustrated in Figure 4.16 show that, for each given ion mobility value, the simulation with bulk fluid flow exhibits faster charging of the EDL. This is the same result seen earlier; Figure 4.16(a), which shows the simulation with ion mobility of 1/3 the sodium ion's actual mobility, was made from the same data set as the first two simulations discussed in section 4.2 above. Figure 4.16 expands on this feature by showing that it remains true for other ion mobilities: bulk fluid motion enhances EDL charging.

Figure 4.16 also shows another feature of this disparity in the charge density curves. The gap between the curves representing charging with and without bulk fluid motion becomes narrower as ion mobility increases. In other words, the advantage conferred by bulk fluid motion is most pronounced when ion mobility is low, and the advantage gets smaller as ion mobility increases. This observation suggests that the charging current can be viewed as having two components: one component that is governed by ion mobility, and another component that is governed by bulk fluid motion.

This can be confirmed by examining the three current plots shown in Figure 4.17(a)-(c). Figure 4.17(a) shows the total current across the electrode pore cross-section as a function of time for the three different ion mobilities. We see that the current in the 1/2 mobility simulation peaks at 57 percent of the current seen in the actual Na^+ mobility simulation, and the current in the 1/3 mobility simulation peaks at 42 percent of the current seen in the actual Na^+ mobility simulation. Figure 4.17(b) shows the current due to convection (bulk fluid motion) only in the three simulations. These convective currents peak at nearly the same level, regardless of the ion mobility. In contrast, the diffusion and

migration current, shown in Figure 4.17(c), exhibits the same trend seen in the total current (Figure 4.17(a)), being directly dependent on the ion mobility value. At the higher diffusion/migration current levels seen in the high-mobility simulations, the 0.1 A convection current represents a lower portion of the total current, hence the narrower gap between the total current in the flow and no-flow simulations for the higher ion mobilities. The consistently higher magnitudes of diffusion and migration currents as compared to convection currents are consistent with observations in prior studies.[2]

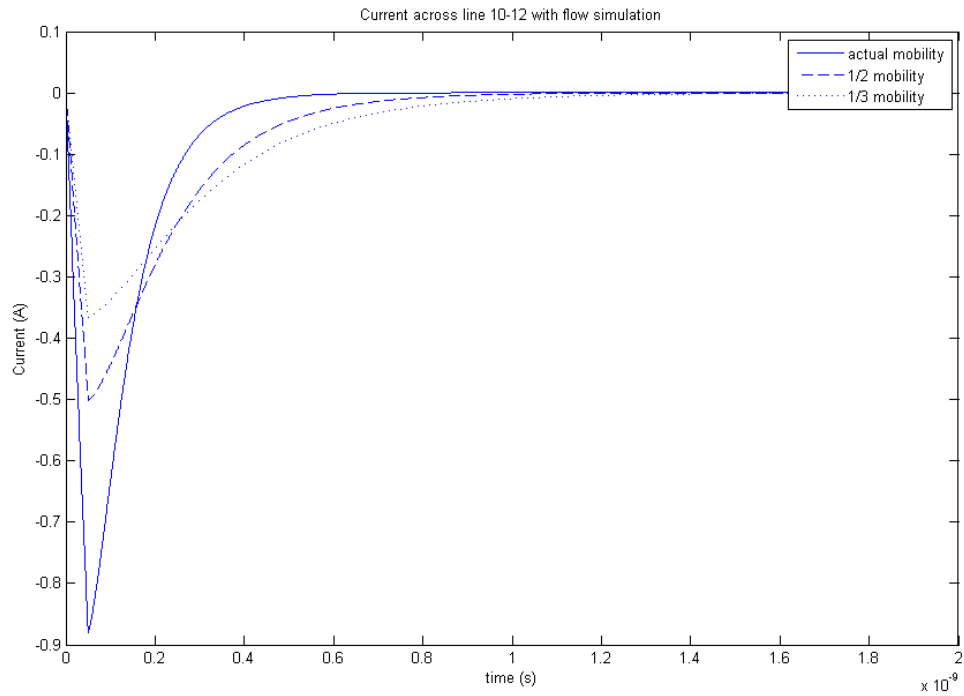
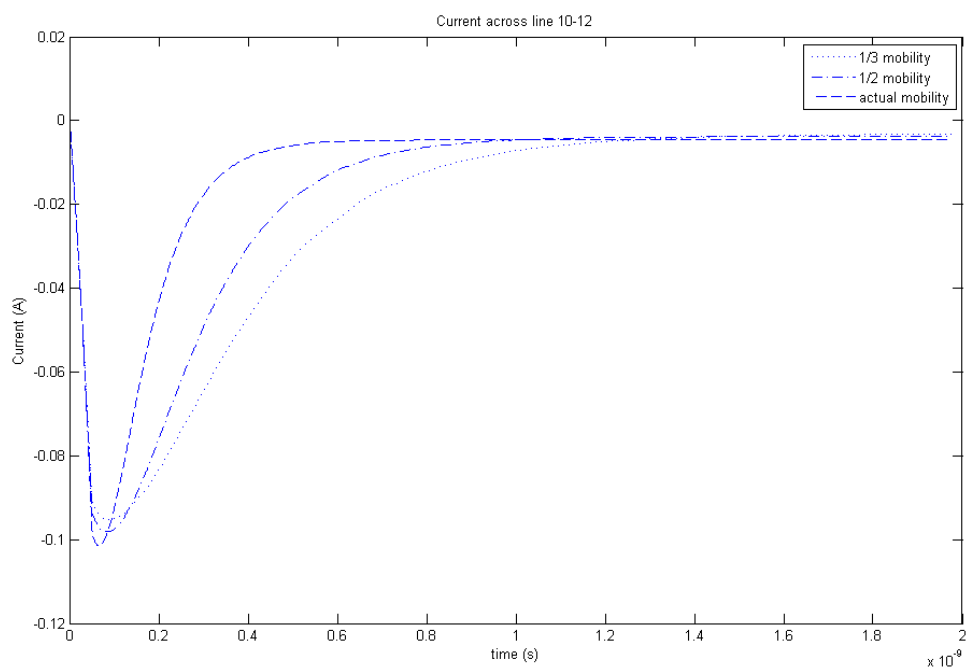
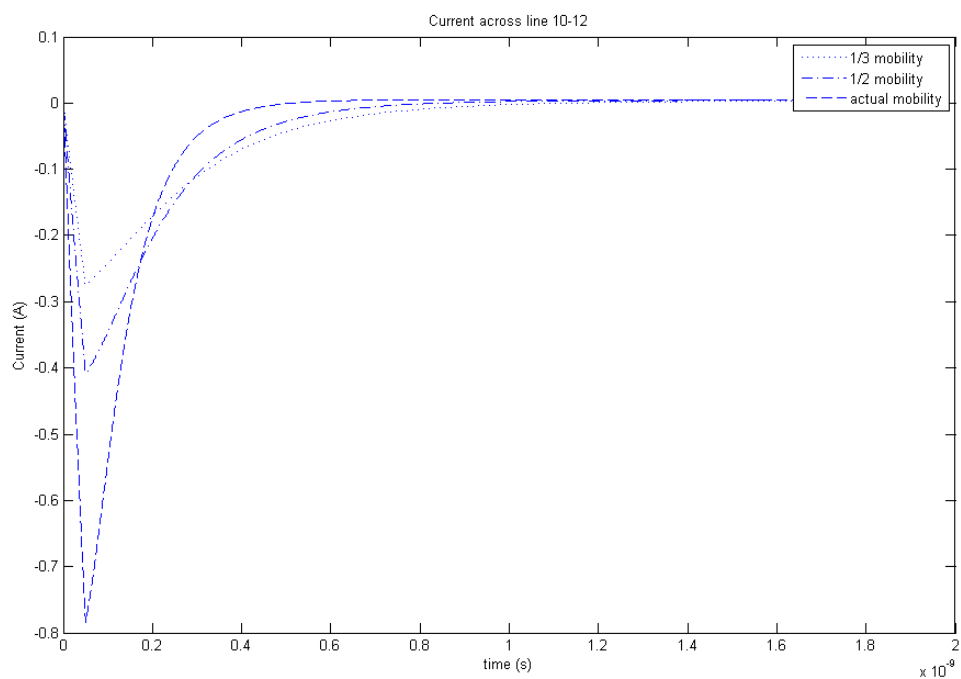


Figure 4.17: Comparison of charging current curves for simulations with bulk flow modeling and different ion mobilities



(b) convection current



(c) diffusion and migration current

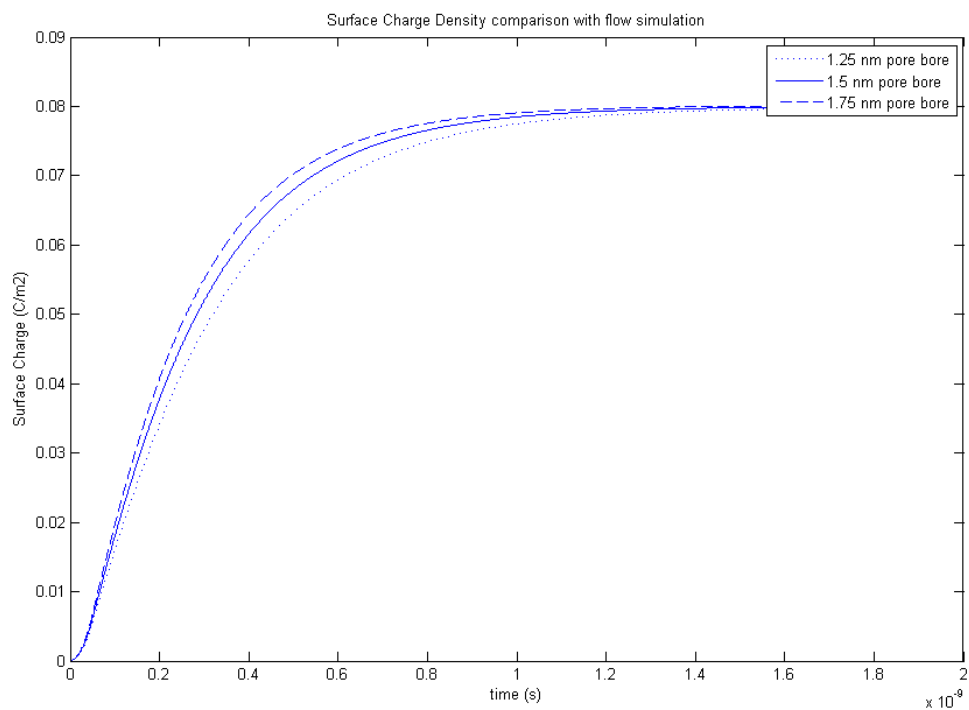
Figure 4.17 (cont'd): Comparison of convection and diffusion/migration charging currents for simulations with bulk flow modeling and different ion mobilities

4.6 Effect of varying the pore bore size

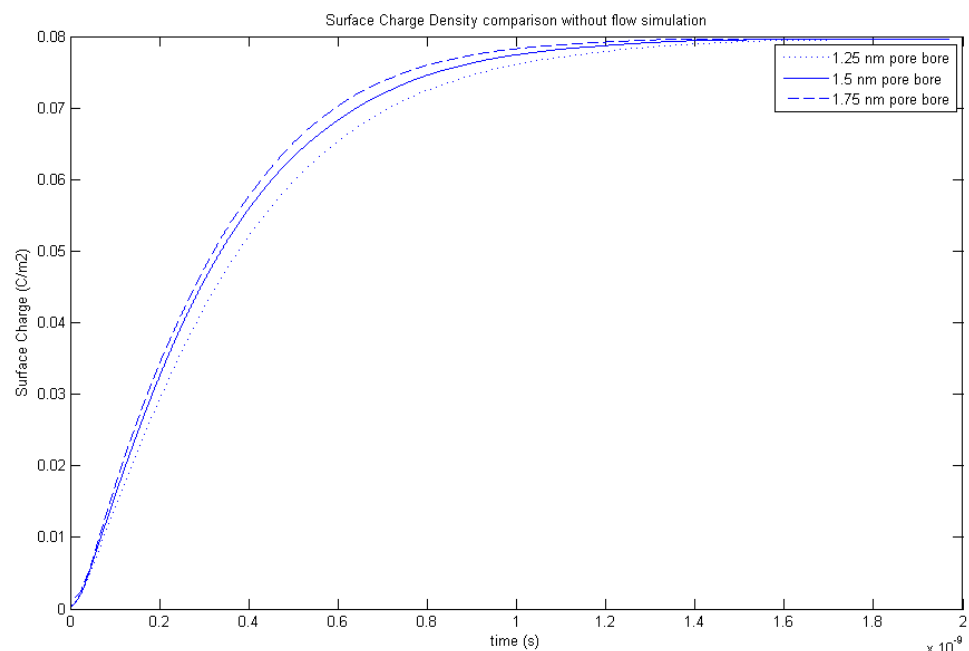
In the next series of simulations, the pore bore was varied. Six simulations were performed in this set to allow each of three pore bore sizes (1.25 nm, 1.5 nm, and 1.75 nm) to be investigated both with and without bulk flow simulation. The values of the other, nonvaried parameters are the same standard control values stated above.

	sim #1	sim #2	sim #3	sim #4	sim #5	sim #6
solvent viscosity	1/10	no flow	1/10	no flow	1/10	no flow
wall slip length	30 nm	no flow	30 nm	no flow	30 nm	no flow
ion mobility	1/3	1/3	1/3	1/3	1/3	1/3
pore bore	1.25 nm	1.25 nm	1.5 nm	1.5 nm	1.75 nm	1.75 nm
pore depth	3 nm	3 nm	3 nm	3 nm	3 nm	3 nm

The electrode charge density curves for these simulations are shown in Figure 4.18.



(a) with bulk flow modeling



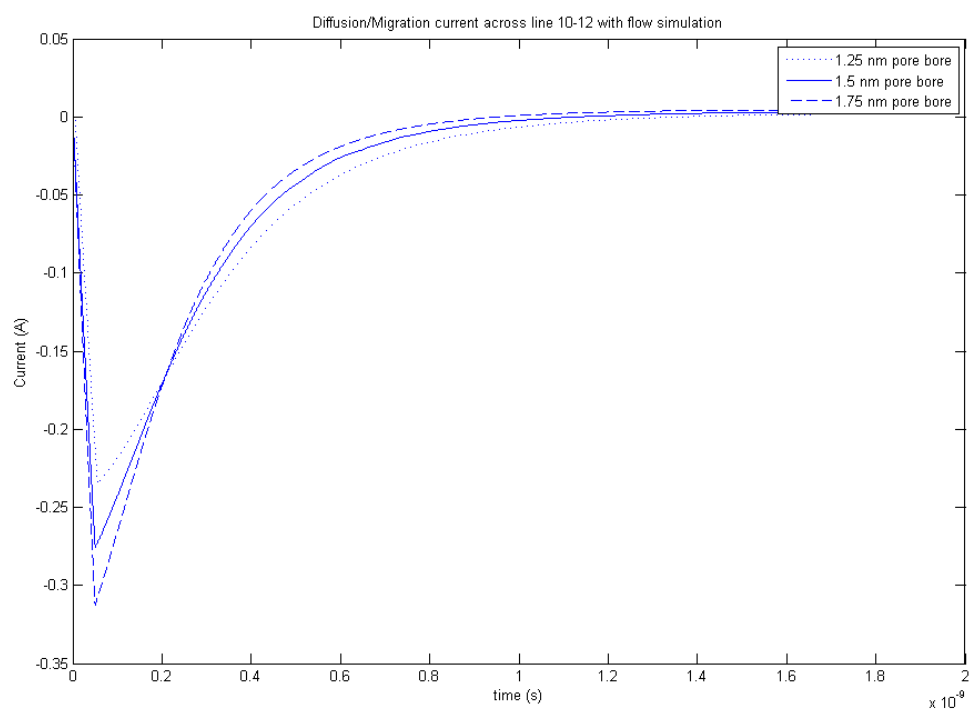
(b) without bulk flow modeling

Figure 4.18: Comparison of electrode charge density curves for simulations with different pore bore sizes

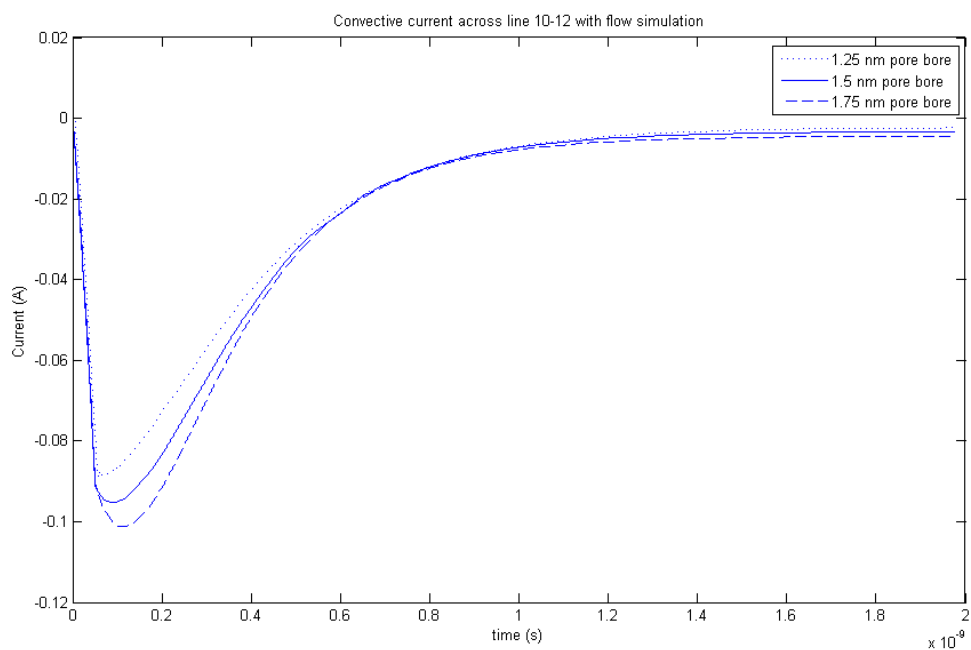
In both comparisons of Figure 4.18, the charging rate is directly related to pore bore size, with the smaller 1.25 pore charging slower than the standard 1.5 nm pore, and the larger 1.75 nm pore charging faster than the standard 1.5 nm pore. This effect is seen with and without bulk flow simulation, which suggests that the larger pore bore boosts charging rate primarily by increasing the diffusion and migration current, which is common to both sets of simulations (flow and no flow) rather than by increasing the convective current, which is present only in the simulations with flow modeling.

We can verify this conjecture by examining the diffusion/migration current and the convective current separately. Figure 4.19(a) shows the diffusion/migration current curves for the different pore bore sizes modeled with flow simulation, and Figure 4.19(b) shows the convective current in these simulations. While the plots reveal that larger pore bore increases both diffusion/migration current and convective current, the effect is much larger for the diffusion/migration current. The diffusion/migration current peaks at 0.235 A in the 1.25 nm pore, as compared to 0.313 A in the 1.75 nm pore, representing an increase of 33 percent. By contrast, the convective current peaks at 0.0889 A in the 1.25 nm pore, as compared to 0.1013 A in the 1.75 nm pore, representing an increase of 12.8 percent.

The dominance of diffusion/migration current, and the relatively minor importance of convective currents in the pore bore comparison, is further confirmed by examining the fluid velocities inside the pore. In all three pores, the fluid velocity on the centerline of the pore peaks at nearly the same value, 2.15 m/s, as expected given the small observed differences in the convective current.



(a) diffusion/migration current



(b) convective current

Figure 4.19: Comparison diffusion/migration current versus convective current with different pore bore sizes

4.7 Effect of varying the pore depth

In the next series of simulations, the pore depth was varied while keeping all other simulation parameters, including the pore bore and all other aspects of the geometry, unchanged. Pore depths of 3 nm and 5 nm were investigated, each with and without bulk flow simulation.

	sim #1	sim #2	sim #3	sim #4
solvent viscosity	1/10	no flow	1/10	no flow
wall slip length	30 nm	no flow	30 nm	no flow
ion mobility	1/3	1/3	1/3	1/3
pore bore	1.5 nm	1.5 nm	1.5 nm	1.5 nm
pore depth	3 nm	3 nm	5 nm	5 nm

The charge density curves comparing the two pore depths are shown in Figure 4.20. We see that EDL charging rate appears to be inversely related to pore depth, with the smaller pore charging faster. Interestingly, this relation holds regardless of whether bulk fluid flow is included in the model. The fact that a smaller pore charges faster than a larger pore when there is no bulk fluid motion suggests that different fluid velocities in the different-sized pores cannot explain this observed phenomenon.

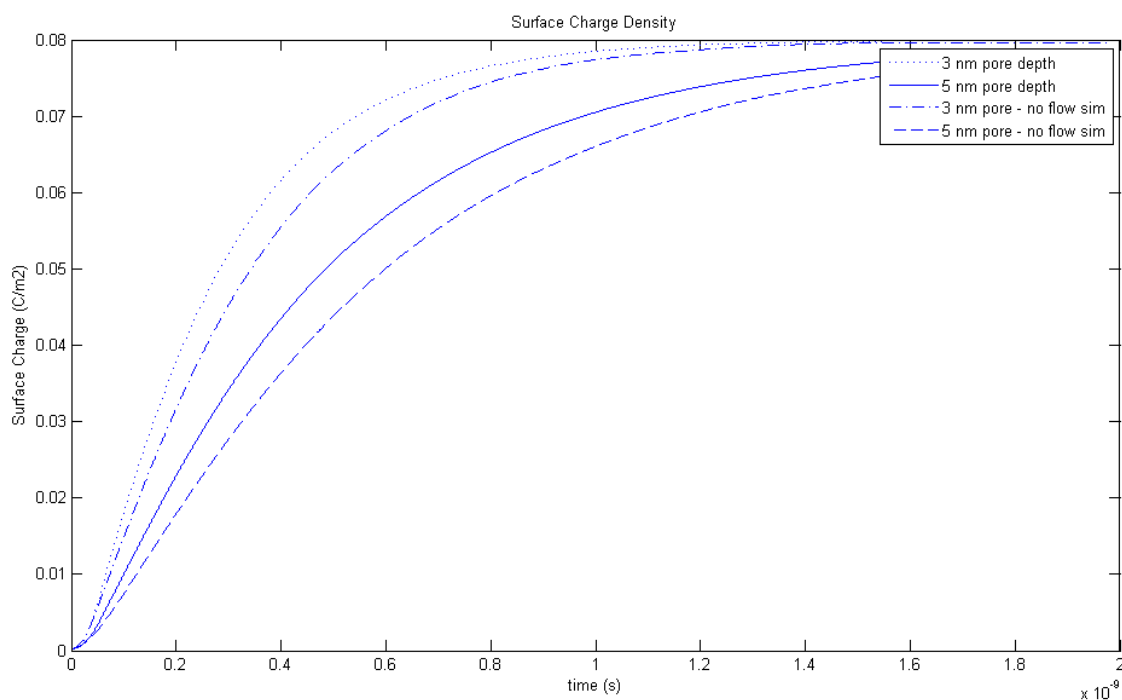


Figure 4.20: Comparison of electrode charge density curves for simulations with different pore depths

Figure 4.21 shows the charging current curves for these simulations, with current measured across the pore cross-section, as before. This comparison of charging current reveals a most unexpected result: the smaller pore exhibits *lower* current levels even while charging *faster* (as revealed by the Figure 4.20 charge density curves). This apparent paradox is explained by the fact that less charge is required to reach the steady state charge density level for the smaller pore. Fewer counterions must enter the pore and accumulate in the EDL in order for a fully-charged condition to be reached, and fewer ions means less current crossing the cross-section of the pore where the data were taken

for Figure 4.21. For the deeper pore, by contrast, more ions are required to fill the larger volume, and they must travel further to reach the deeper extent of the pore as the EDL is built up. We would therefore expect to find fluid velocities to be uniformly greater across the deeper pore, notwithstanding the lower current levels seen in that case. This is indeed confirmed in the velocity profiles taken across the pore at different times during the charging process, as shown in Figure 4.22.

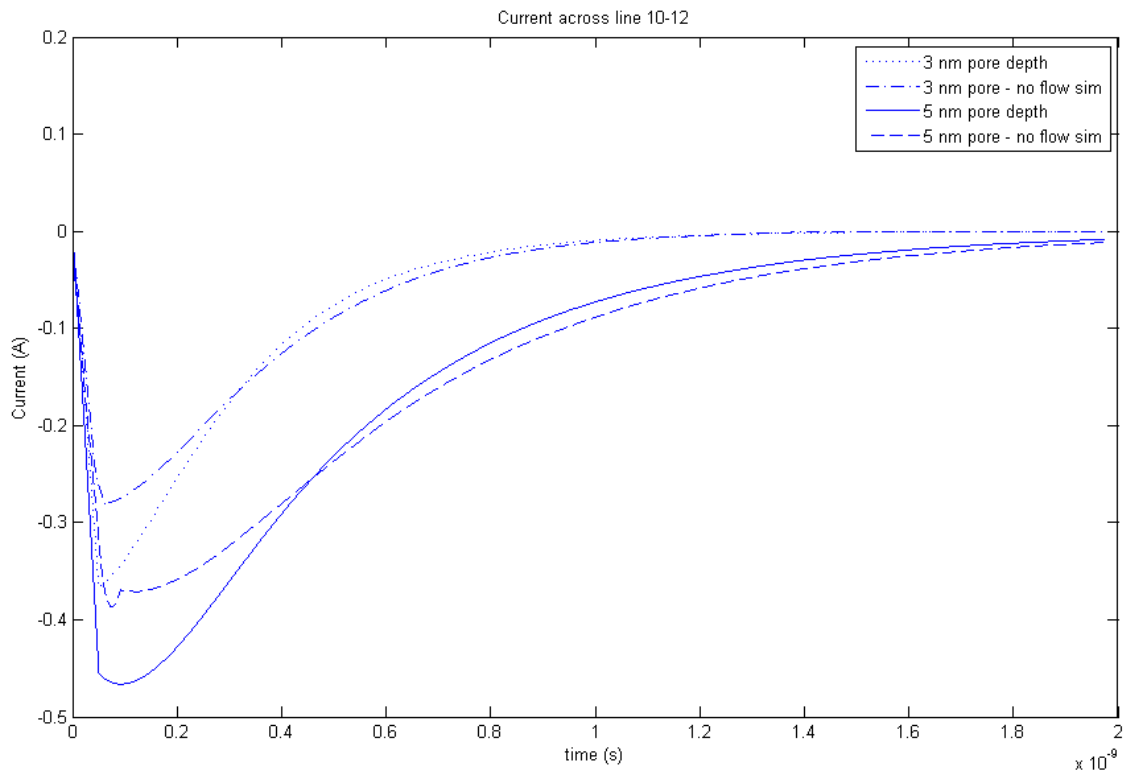


Figure 4.21: Comparison of charging current curves for simulations with different pore depths

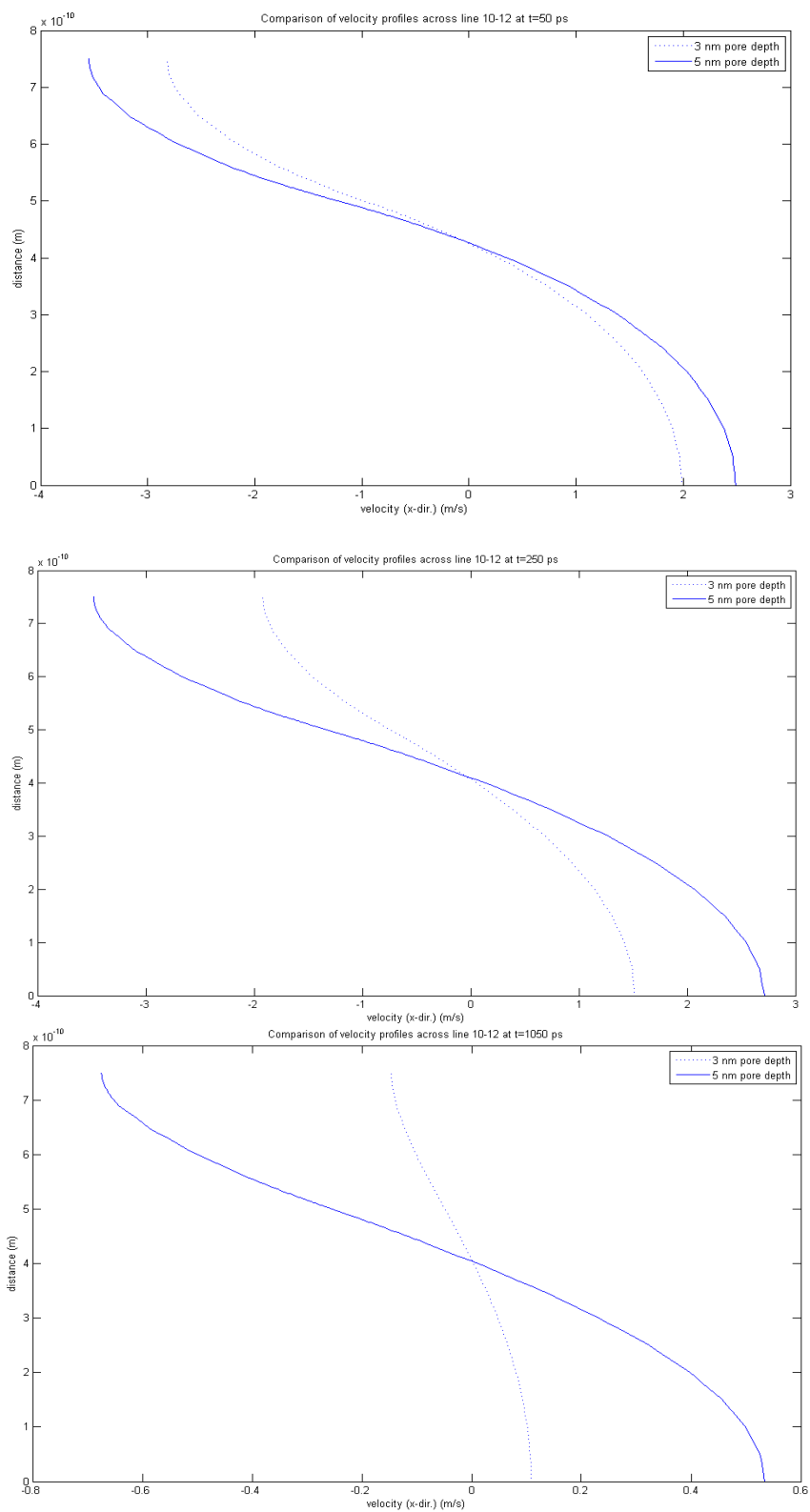


Figure 4.22: Comparison of velocity profiles across pores of different depths

4.8 Effect of varying the solvent density

In the next series of simulations, the solvent density was varied while keeping all other simulation parameters unchanged. Density values of 1/10, 1/3, and actual density of water were used.

	sim #1	sim #2	sim #3	sim #4
solvent density	actual - water	1/3	1/10	no flow
solvent viscosity	1/10	1/10	1/10	no flow
wall slip length	30 nm	30 nm	30 nm	no flow
ion mobility	1/3	1/3	1/3	1/3
pore bore	1.5 nm	1.5 nm	1.5 nm	1.5 nm
pore depth	3 nm	3 nm	3 nm	3 nm

Figure 4.23 shows the electrode charge density curves for this set of simulations, and Figure 4.24 shows the fluid velocity profiles across the pore cross-section at different times for the simulations with bulk flow modeling.

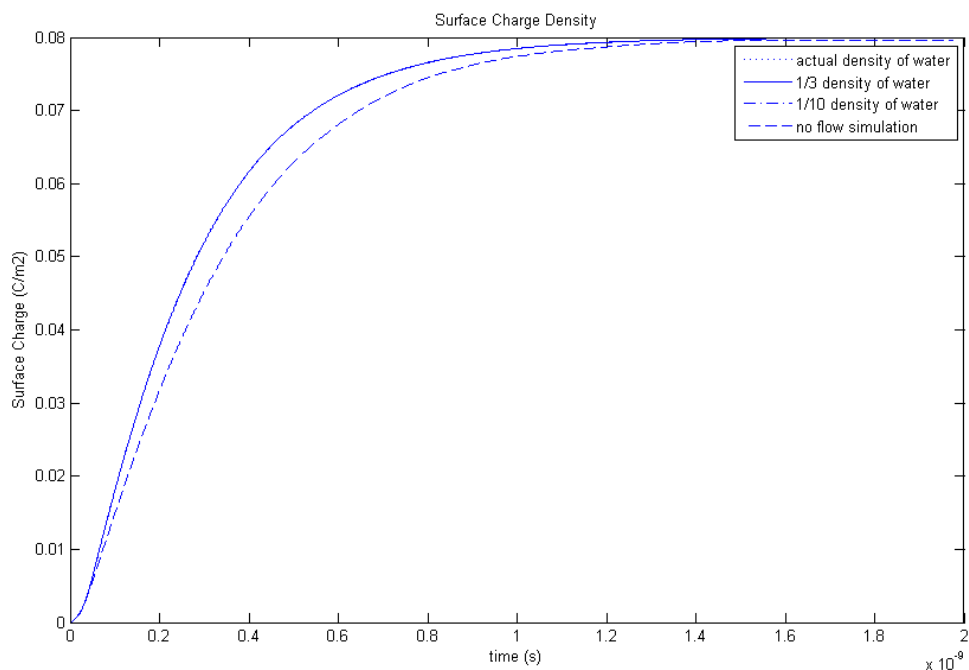


Figure 4.23: Comparison of electrode charge density curves for simulations with different solvent densities

These plots reveal no difference in the charging rate for the three simulations with different solvent densities, and nearly imperceptible differences in the velocity profiles. These results are consistent with the low-Reynolds number nature of the flow in these simulations. As discussed above in Chapter 3, the Reynolds number for these flows is approximately 0.0225. At this magnitude, even a change of fluid density (and hence Reynolds number) by a factor of 10 leaves the Reynolds number very small, thus rendering inertial effects inconsequential for these flows. Therefore, fluid density does not have a measureable impact on the fluid flow or charging kinetics in these nanoscale flows.

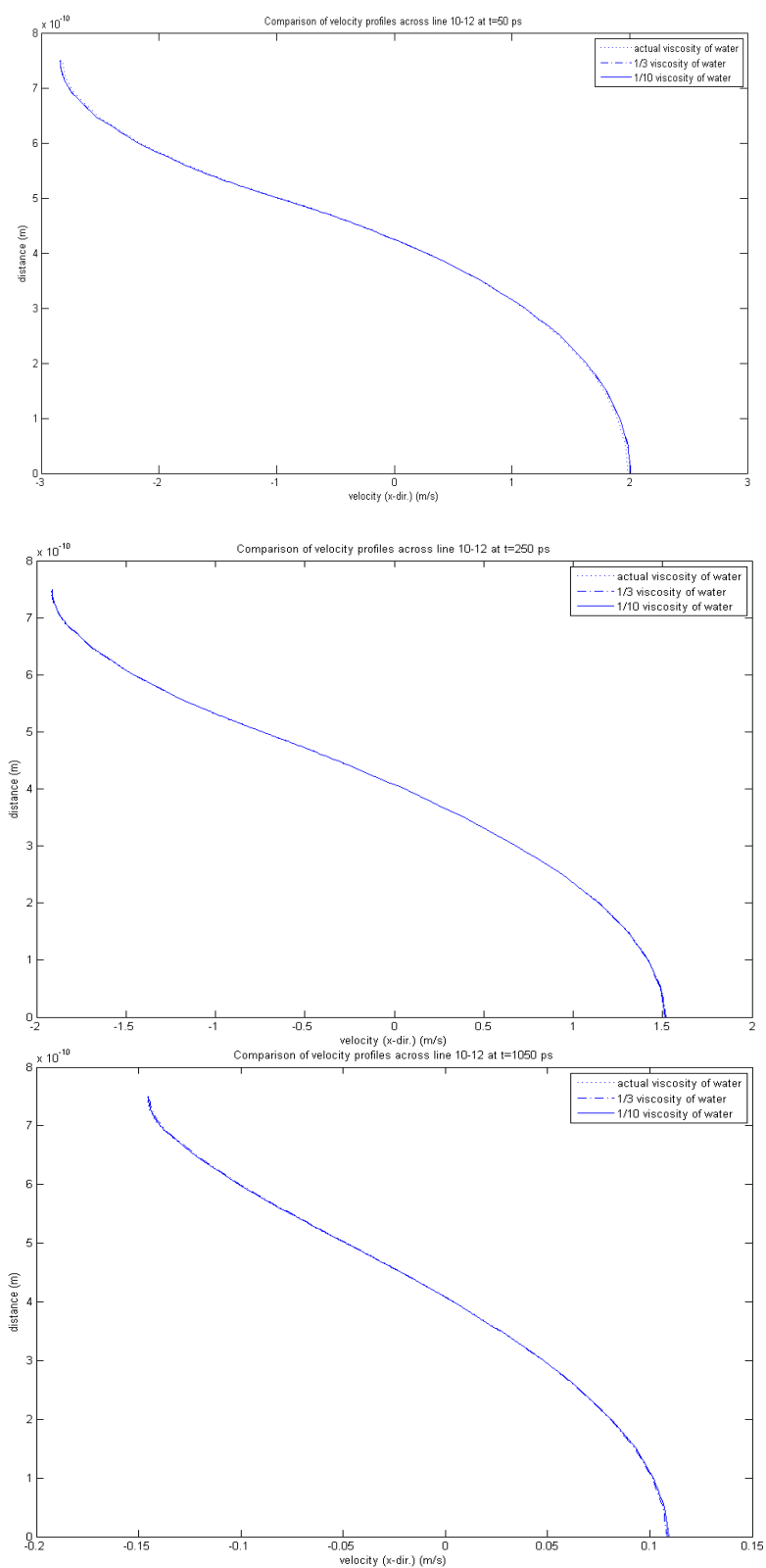


Figure 4.24: Comparison of velocity profiles with different solvent densities

CHAPTER 5

CONCLUSIONS

The investigation presented in this thesis was designed to simulate the charging of the EDL using a continuum model based on the PNP equations, with the addition of bulk fluid flow modeling using the Navier-Stokes Equations. The electrochemical devices in which EDLs form necessarily contain a fluid (whether aqueous or ionic liquid) medium carrying the ions that constitute the EDL; therefore, it is reasonable to suspect that the motion of this fluid would affect the EDL charging kinetics. As this fluid flow modeling has not previously been performed in EDL charging simulations, the present investigation was intended to fill this gap and enhance understanding of the charging kinetics in the entire EDL/electrolyte system.

The present investigation consists of a parametric study to investigate the different physical parameters of the EDLC apparatus to determine the effect of each parameter on the EDL charging kinetics. At the outset, it was observed that the addition of Navier-Stokes bulk flow modeling to the PNP model does indeed increase the charging current flowing into the electrode pores, thus causing charge to accumulate in the EDL faster than observed without the flow modeling. Because a bulk fluid medium is inherent in all EDL devices, this result suggests that the flow modeling could provide

more accurate and realistic data analyzing the performance and design of electrochemical devices.

The parametric study established that fluid viscosity has a direct impact on the EDL charging rate, with lower-viscosity fluids allowing higher velocities to be attained, which results in a greater convective component to the charging current. This result confirms that low-viscosity solvents, such as the widely-used acetonitrile (ACN), provide performance benefits in electrochemical devices.

Different ion electrokinetic mobilities were studied, and it was found that the addition of flow modeling has a more pronounced effect on the EDL charging rate for lower-mobility ions. Lower-mobility ions produce smaller diffusion and migration currents, which makes the convective current larger as a percentage of total current. Nevertheless, lower ion mobility significantly reduce the total charging current and hence lengthen EDL charging times, making them unattractive for most electrochemical devices.

Greater wall slip was found to enhance the convective current and, therefore, the total charging current. This result suggests that efforts to choose materials and precise machining and manufacturing processes to minimize wall friction can improve device performance.

Electrode pore size was found to have perhaps the most significant impact on EDL charging rate. Shallower pores were found to charge significantly faster than deep pores. This result can be understood in terms of EDL structure and pore geometry; with shallow pores requiring fewer ions to reach the full steady-state charge density.

Increasing the pore width (or bore) results in a corresponding increase in the charging rate which, in this case, is caused by increased diffusion and migration current across the greater pore cross-sectional area.

We have seen that the fundamental parameters governing the EDLC apparatus provide a useful testing ground for evaluating the effect of bulk flow modeling on the EDL charging kinetics. Variation of different parameters can produce faster charging rates, usually accompanied by higher charging currents, with the relative size of the flow-based convective current contribution depending on which parameters are varied. These results illustrate the important role of fluid flow in EDL devices and suggest factors to be considered in the design and analysis of such devices when bulk fluid flow is included in the model.

APPENDIX A

IMPLEMENTATION OF THE APPLIED POTENTIAL FUNCTION IN COMSOL

As mentioned above in Chapter 3, the applied electric potential across the electrodes was varied in order to create controlled conditions to permit accurate assessment of the charge and fluid velocity data. Each simulation began with zero applied potential in order to allow the ions in the electrolyte solution to reach an equilibrium distribution. This Phase 1 typically lasted around 1 ns. The applied potential was then increased linearly to 1 V over a time of 50 ps in order to eliminate discontinuities in the variables and instabilities in the COMSOL solver. The potential was then held at 1 V for the remainder of the simulation to allow the EDL to reach its steady-state charged condition.

The potential function described here was implemented in COMSOL by defining parameters to specify the time marks where the potential was changed. As an example, the parameter *mark1* could be used to specify the time when the linear ramp-up to 1 V began, and the parameter *mark2* could be used to specify the time when the potential is to reach 1 V. Then the function to specify the applied potential throughout the time of the simulation was coded as follows:

$$V = 0 + (\text{mark1} \leq t) * (t < \text{mark2}) * V_{\text{final}} / (\text{mark2} - \text{mark1}) * (t - \text{mark1}) + (\text{mark2} \leq t) * V_{\text{final}}$$

The first term, 0, just ensures that COMSOL starts at 0 V. The second term provides the linear increase in potential, where the rate of change is the difference in potential ($V_{\text{final}} -$

0) over the time interval for the change ($\text{mark2} - \text{mark1}$). The linear increase with time over this interval is accomplished by the factor $(t - \text{mark1})$. The factors $(\text{mark1} \leq t)$ and $(t < \text{mark2})$ are conditional Boolean expressions (which have the value 0 or 1, depending on whether the conditional statement is true) that operate to make this linear increase happen only when the time variable t is between mark1 and mark2 (making both conditional statements true and thus having the value 1). The third term in the expression holds the potential at V_{final} at all times after than mark2 ; this is the constant potential maintained after the linear ramp-up for the remainder of the simulation.

The potential function generated by this COMSOL expression is plotted in Figure A.1 below.

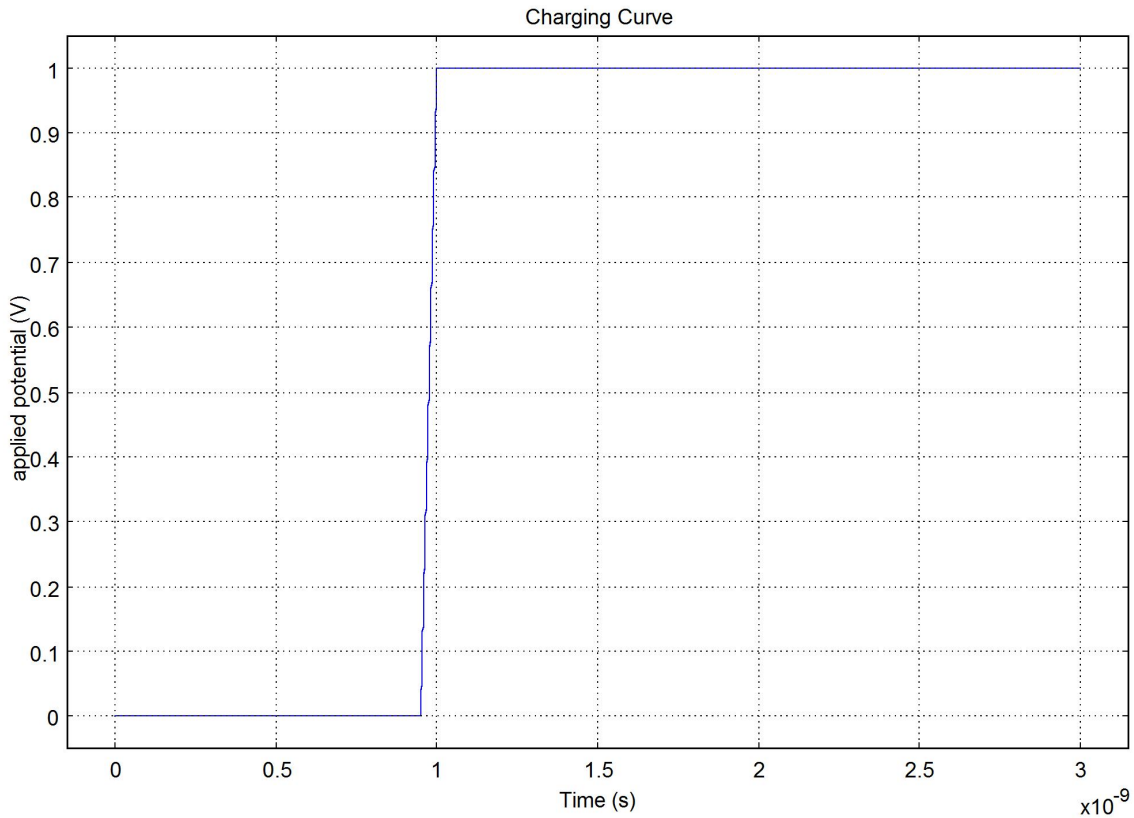


Figure A.1: Applied Potential Function

ENDNOTES AND REFERENCES

- [1] Y. Ai and S. Qian. Electrokinetic particle translocation through a nanopore. *Phys. Chem. Chem. Phys.*, 13, 4060-4071 (2011).
- [2] F. Baldessari. Electrokinetics in Nanochannels, Part II: Mobility dependence on ion density and ionic current measurements. *J. Colloid & Interface Sci.*, 325, 539-546 (2008).
- [3] A.J. Bard and L.R. Faulkner, ed. *Electrochemical Methods: Fundamentals and Applications*. John Wiley & Sons, Inc., New York, second edition, 2001.
- [4] L.B. Bhuiyan and D. Henderson. A local, semi-empirical contact condition for the charge profile in an electric double layer with size-asymmetric ions at low electrode charge: comparison with simulations. *Molecular Simulation*, Vol. 37, No. 4, 269-276 (2011).
- [5] R. Bird, W. Stewart, and E. Lightfoot. *Transport Phenomena*. John Wiley & Sons, Inc., New York, second edition, 2002.
- [6] A.M. Bittner, M. Zhu, Y. Yang, H.F. Waibel, M. Konuma, U. Starke, and C.J. Weber. Ageing of electrochemical double layer capacitors. *J. Power Sources*, 203, 262-273 (2012).
- [7] K. Bohinc, A. Shrestha, M. Brumen, and S. May. Poison-Helmholtz-Boltzmann model of the electric double layer: Analysis of monovalent ionic mixtures. *Phys. Rev. E*, 85, 031130 (2012).
- [8] R.D. Branam and M.M. Micci. Comparison of wall models for the molecular dynamics simulation of microflows. *Nanoscale and Microscale Thermophysical Engineering*, Vol. 13, 1-12 (2009).
- [9] H. Butt, K. Graf, and M. Kappl. *Physics and Chemistry of Interfaces*. Wiley-VCH Verlag & Co., New York, 2003.
- [10] P.J. Cadusch, B.D. Todd, J. Zhang, and P.J. Davis. A non-local hydrodynamic model for the sheer viscosity of confined fluids: analysis of a homogeneous kernel. *J. Phys. A: Math. Theor.*, 41 (2008) 035501.
- [11] C. Cagle, G. Feng, R. Qiao, J. Huang, B.G. Sumpter, and V. Meunier. Structure and charging kinetics of electrical double layers at large electrode voltages. *Microfluid Nanofluid*, 8:703-708 (2010).

- [12] J. Chmiola, G. Yushin, Y. Gogotsi, C. Portet, P. Simon, and P.L. Taberna. Anomalous Increase in Carbon Capacitance at Pore Sizes Less Than 1 Nanometer. *Science*, Vol. 313, No. 5794, 1760-1763 (2006).
- [13] M.H. Ervin, B.S. Miller, B. Hanrahan, B. Mailly, and T. Palacios. A comparison of single-wall carbon nanotube electrochemical capacitor electrode fabrication methods. *Electrochimica Acta*, 65, 37-43 (2012).
- [14] K. Falk, F. Sedlmeier, L. Joly, R.R. Netz, and L. Bocquet. Molecular Origin of Fast Water Transport in Carbon Nanotube Membranes: Superlubricity versus Curvature Dependent Friction. *Nano Lett.*, 10, 4067-4073 (2010).
- [15] W.R. Fawcett and T.G. Smagala. Examination of ion size effects on the potential drop across the diffuse layer using Monte Carlo simulations. *Electrochimica Acta*, 53, 5136-5141 (2008).
- [16] S.W. Feldberg. On the dilemma of the use of the electroneutrality constraint in electrochemical calculations. *Electrochemistry Communications*, 2, 453-456 (2003).
- [17] G. Feng, J. Huang, B. Sumpter, V. Meunier, and R. Qiao. Structure and dynamics of electrical double layers in organic electrolytes. *Phys. Chem. Chem. Phys.*, 12, 5468-5479 (2010).
- [18] L. Gong and J. Wu. Resistance Effect of Electric Double Layer on Liquid Flow in Microchannel. *Applied Math. & Mech.*, 27(10), 1391-1398 (2010).
- [19] D. Huang, C. Sendner, D. Horinek, R. Netz, and L. Bocquet. Water Slippage versus Contact Angle: A Quasiuniversal Relationship. *Phys. Rev. Lett.* 101, 226101 (2008).
- [20] J. Huang, B. Sumpter, and V. Meunier. A Universal Model for Nanoporous Carbon Supercapacitors Applicable to Diverse Pore Regimes, Carbon Materials, and Electrolytes. *Chem. Eur. J.* 14, 6614-6626 (2008).
- [21] X. Jiang and R. Qiao. Electrokinetic Transport in Room-Temperature Ionic Liquids: Amplification by Short-Wavelength Hydrodynamics. *J. Phys. Chem. C*, 116 (1), 1133-1138 (2012).
- [22] V.O. Khavrus, M. Weiser, M. Fritsch, R. Ummethala, M.G. Salvaggio, M. Schneider, M. Kusnezoff, and A. Leonhardt. Application of Carbon Nanotubes Directly Grown on Aluminum Foils as Electric Double Layer Capacitor Electrodes. *Chem. Vapor Dep.*, 18, 53-60 (2012).

- [23] S. Koneshan, J.C. Rasaiah, R.M. Lynden-Bell, and S.H. Lee. Solvent structure, dynamics, and ion mobility in aqueous solutions at 25 °C. *J. Phys. Chem. B*, 102- 4193-4204 (1998).
- [24] P. Kossyrev. Carbon black supercapacitors employing thin electrodes. *J. Power Sources*, 201, 347-352 (2012).
- [25] Y. Li, J. Xu, and D. Li. Molecular dynamics simulation of nanoscale liquid flows. *Microfluid Nanofluid*, 9:1011-1031 (2010).
- [26] J. Lim. J.D. Whitcomb, J.G. Boyd, and J. Varghese. Effect of electrode pore geometry modeled using Nernst-Planck-Poisson-modified Stern Layer model. *Comput. Mech.* 43: 461-475 (2009).
- [27] M. Majumder, N. Chopra, and B. Hinds. Mass Transport Through Carbon Nanotube Membranes in Three Different Regimes: Ionic Diffusion and Gas and Liquid Flow. *ACS Nano*, Vol. 5, No. 5, 3867-3877 (2011).
- [28] Y. Marcus. Thermodynamics of ion hydration and its interpretation in terms of a common model. *Pure & Applied Chem.*, Vol. 59, No. 9, 1093-1101 (1987).
- [29] Y. Marcus. Ionic radii in aqueous solutions. *Chem. Rev.*, 88, 1475-1498 (1988).
- [30] R. Mukherjee, S. Das, A. Das, S. Sharma, A. Raychaudhuri, and A. Sharma. Stability and Dewetting of Metal Nanoparticle Thin Polymer Films: Control of Instability Length Scale and Dynamics. *ACS Nano*, Vol. 4, No. 7, 3709-3724 (2010).
- [31] T.G. Myers. Why are slip lengths so large in carbon nanotubes? *Microfluid Nanofluid*, 10:1141-1145 (2011).
- [32] C. Ng and C.Y. Wang. Apparent slip arising from Stokes shear flow over a bidimensional patterned surface. *Microfluid Nanofluid*, 8:361-371 (2010).
- [33] S. Pennathur and J.G. Santiago. Electrokinetic Transport in Nanochannels: 1. Theory. *Anal. Chem.*, 77, 6772-6781 (2005).
- [34] R. Qiao and N.R. Aluru. Scaling of Electrokinetic Transport in Nanometer Channels. *Langmuir*, 21, 8972-8911 (2005).
- [35] S. Rajamani, T. Ghosh, and S. Garde. Size dependent ion hydration, its asymmetry, and convergence to macroscopic behavior. *J. Chem. Phys.*, Vol. 120, No. 9, 4457-4466 (2004).

- [36] D.B. Robinson. Optimization of power and energy densities in supercapacitors. *J. Power Sources*, 195, 3748-3756 (2010).
- [37] C. Sendner, D. Horinek, L. Bocquet, and R. Netz. Interfacial Water at Hydrophobic and Hydrophilic Surfaces: Slip, Viscosity, and Diffusion. *Langmuir* 25(18), 10768-10781 (2009).
- [38] W. Silvestre-Alcantara, L. Bhuiyan, C. Outhwaite, and D. Henderson. A Modified Poisson-Boltzmann Study of the Singlet Ion Distribution at Contact with the Electrode for a Planar Electric Double Layer. *Collect. Czech. Chem. Comm.*, Vol. 75, No. 4, 425-446 (2010).
- [39] B. Skinner, T. Chen, M.S. Loth, and B.I. Shklovskii. Theory of volumetric capacitance of an electric double-layer supercapacitor. *Physical Review E*, 83, 056102 (2011).
- [40] V. Srinivasan and J.W. Weidner. Mathematical Modeling of Electrochemical Capacitors. *J. Electrochem. Soc.*, 146 (5) 1650-1658 (1999).
- [41] B.D. Todd and J.S. Hansen. Nonlocal viscous transport and the effect on fluid stress. *Physical Review E*, 78, 051202 (2008).
- [42] M. Urbakh, L. Daikhin, and J. Klafter. Sheared liquids in the nanoscale range. *J. Chem. Phys.*, Vol. 103, 10707 (1995).
- [43] M.W. Verbrugge and P. Liu. Microstructural Analysis and Mathematical Modeling of Electric Double-Layer Supercapacitors. *J. Electrochem. Soc.*, 152 (5) D79-D87 (2005).
- [44] K. Xie, X. Qin, X. Wang, Y. Wang, H. Tao, Q. Wu, L. Yang, and Z. Hu. Carbon Nanocages as Supercapacitor Electrode Materials. *Adv. Mater.*, 24, 347-352 (2012).
- [45] T. Yan, C.J. Burnham, M.G. Del Popolo, and G.A. Voth. Molecular Dynamics Simulation of Ionic Liquids: The Effect of Electronic Polarizability. *J. Phys. Chem. B*, Vol. 108, No. 32, 11877-11881 (2004).
- [46] Z. Yuan, A.L. Garcia, G.P. Lopez, and D.N. Petsev. Electrokinetic transport and separations in fluidic nanochannels. *Electrophoresis*, 28, 595-610 (2007).